Evaluating Chemoradiation Resistance using 18F-FDG PET/CT in Murine Head and Neck Squamous Cell Carcinoma

by

Casey Claire Heirman

Graduate Program in Medical Physics
Duke University

Defense Date: March 15, 2024

Approved:

Kyle Lafata, Advisor

Yvonne Mowery

Chunhao Wang

Thesis submitted in partial fulfillment of the requirements for the degree of Master of Science in the Graduate Program in Medical Physics in The Graduate School of Duke University
2024

ABSTRACT

Evaluating Chemoradiation Resistance using 18F-FDG PET/CT in Murine Head and Neck Squamous Cell Carcinoma

by

Casey Claire Heirman

Graduate Program in Medical Physics
Duke University

Defense Date: March 15, 2024

Approved:

Kyle Lafata, Advisor

Yvonne Mowery

Chunhao Wang

An abstract of a thesis submitted in partial fulfillment of the requirements for the degree of Master of Science in the Graduate Program in Medical Physics in The Graduate School of Duke University
2024

Abstract

Purpose: There is an urgent need for enhanced prognostic tools and insights into the biology and biomarkers of chemoradiation resistance. The purpose of this research is to identify prognostic radiomic features on 18F-FDG micro-PET/CT images for the response to chemoradiation in mouse models of head and neck squamous cell carcinoma (HNSCC).

Methods: Two orthotopic murine human papillomavirus (HPV)-negative (MOC1, MOC2) models and one HPV-positive HNSCC model (MLM1) were utilized. Oral cavity tumors were induced by injecting HNSCC cells into the buccal mucosa of C57BL/6J mice. Bidirectional caliper tumor measurements were conducted thrice weekly with chemoradiation initiated once tumors exceeded $50mm^3$: cisplatin (5 mg/kg, intraperitoneal) and image-guided radiation therapy (8 Gy) on days 0 and 7. On day 14, 18F-FDG PET/CT imaging was performed. Mice were euthanized when they reached humane endpoint (tumor >12mm, any dimension). Tumors were segmented on PET/CT, and volume, SUVmean, and SUVmax were extracted. Liver regions of interest were segmented for normalization of tumor SUVmax to liver SUVmean. Treatment response was evaluated using tumor size on day 10 relative to day 0. Tumor growth and survival were compared across models (Kruskal-Wallis with Tukey's post hoc test) and based on image feature parameters (Mann-Whitney U test). The associations between survival, SUVmax, and tumor volumes were analyzed by Cox proportional hazards model and Kaplan-Meier curves with log-rank test.

Results: 121 mice underwent treatment and imaging. Univariate analysis showed that median tumor volume and SUVmax were significantly associated with survival and treatment response ($p<0.05$). The Cox model indicated a significant difference in survival probability based on risk

score values derived from the model's coefficients estimating their relative risk of time-to-event ($p<0.0001$).

Conclusion: These results suggest that image features on 18F-PET/CT can provide prognostic insight into treatment response and survival in preclinical HNSCC models, providing a platform for further studies to improve understanding of the biological underpinnings of radiomic expression associated with chemoradiation resistance.

Dedication

I am incredibly grateful for the support I have received from my friends and family to follow my dreams and pursue a life in science.

To my dad, Amy, my mom, and Sandy, thank you for shaping me into the person I am and always having faith in me.

I am also so grateful for the Duke Medical Physics community and the friends and colleagues I have met here that I will have for the rest of my career. I especially could not have done this without Jessie and Tyler, whom I owe endless thanks to for helping me every time I needed it, academically or emotionally.

To Chantelle, Cam, Ali, and Bennett, you have stuck with me through it all, and I hope you are ready to stick through it some more. Every day my goal is to make you guys proud.

To Garrett, for making my transition to North Carolina so much easier and taking care of me and Niko during our time here.

Niko, I would be nowhere without my emotional support kitty. Thank you for being the best little guy known to man. Thank you for keeping me company and always keeping me sane and full of love.

And lastly, thank you to all the laboratory mice and animals who have dedicated their lives for the betterment of both human and animal society. Your sacrifices do not go unseen, and I know there is a special place in heaven for all of you.

Contents

Abstract iv

List of Tables x

List of Figures xi

Acknowledgements xiii

1. Introduction and Background 1

1.1 Significance and Motivation 1

1.1.1 HPV-Positive HNSSC 2

1.2 Relevant Imaging Modalities 2

1.2.1 Computed Tomography Imaging 2

1.2.2 ^{18}F-Fluorodeoxyglucose Positron Emission Tomography Imaging 3

1.2.2.1 Standardized Uptake Values, SUVmax and SUV Normalization 4

1.3 Advanced Analytical Computation Techniques in Oncology 5

1.3.1 Radiomics 5

1.3.1.1 Histogram Features 5

1.3.1.2 Shape-based Features 6

1.3.2 Cox Proportional Hazards Model 6

1.4 Relevant Clinical Background 7

1.4.1 Clinical Trial Investigating Prognostic Radiomic Markers in Head and Neck Cancer 7

1.4.2 Tumor Models Used in HNSSC Research 7

1.4.2.1 C57BL/6J Mice 7

1.4.2.2 MOC1 and MOC2 Cell Lines 8

1.4.2.3 MLM1 Cell Line 9

2. Methods 10
2.1 Experimental Design 10
2.1.1 Models, Cell Culture, and Induction 10
2.1.1.1 Tumor Models and Cell Culture 10
2.1.1.2 Induction 11
2.1.2 Monitoring the Mice 12
2.1.3 Chemoradiation Treatment 13
2.1.4 ^{18}F FDG PET/CT Imaging 13
2.1.5 Humane Endpoints 13
2.2 Data Analysis 14
2.2.1 Tumor Model Growth, Response, and Survival Analysis 14
2.2.2 Image Feature Analysis 15
2.2.2.1 Segmentation of Tumor and Liver Regions of Interest and Image Feature Extraction 15
2.2.2.2 Univariate Response Analysis 16
2.2.2.3 Univariate Survival Analysis 17
2.2.2.4 Univariate Image Features and Tumor Model Analyses 18
2.2.2.5 Multivariate Survival Analysis 18
3. Results 20
3.1 Tumor Model Growth, Response, and Survival Analysis 20
3.2 Image Feature Analysis 24
3.2.1 Segmentation Results 24
3.2.2 Univariate Response Analysis 27
3.2.3 Univariate Survival Analysis 30

3.2.4 Univariate Image Features and Tumor Model Analyses 32
3.2.5 Multivariate Survival Analysis - Cox Proportional Hazards Model 35
4. Discussion 37
4.1 Tumor Model Growth, Response, and Survival 37
4.2 Image Feature Analysis 37
4.2.1 Segmentation Results 37
4.2.2 Univariate Response and Survival Analysis 38
4.2.3 Univariate Image Features and Tumor Model Analyses 39
4.2.4 Multivariate Survival Analysis - Cox Proportional Hazards Model 41
4.3 Future Directions 41
4.3.1 Multiscale Analyses 41
4.3.2 Future Mouse Models 43
5. Conclusions 45
Appendix A 46
A.1 Media Recipes and Stock Solutions 46
Works Cited 50

List of Tables

Table 1. Reference Hounsfield units and resultant thresholding range selected for the ROI segmentation process. 16

Table 2. Covariates analyzed in the univariate response analysis and corresponding statistical test employed. 17

Table 3. Median survival time based on tumor model. 21

Table 4. Descriptive statistics regarding image features extracted from the PET/CT contoured regions of interest in the tumor and liver, rounded to two decimals, for the complete dataset. 26

Table 5. Statistical parameters analyzing the coefficients of variation for all liver segmentation SUV measurements. 35

Table 6. Cox proportional hazards model coefficients for covariates and resultant hazard ratios. 36

List of Figures

Figure 1. The experimental pipeline. 10

Figure 2. Dimensions measured externally using calipers to allow for a cylindrical volume approximation. 12

Figure 3. Tumor growth trends using normalized tumor volume post first treatment: comparison of the three tumor models. 20

Figure 4. Survival probability post treatment based on tumor model. 21

Figure 5. Normalized tumor growth based on treatment response. 22

Figure 6. Tumor growth based on response showing high-, mid-, and low-responders. 23

Figure 7. Distribution of response within each tumor model. 24

Figure 8. Example segmentation result. 25

Figure 9. Example PET/CT slice with anatomy labeled. 26

Figure 10. Comparing the results of the two volume measurement methods on the same or closest neighboring days. 27

Figure 11. Volume of segmented ROIs on the PET/CT scans versus treatment response group. 28

Figure 12. SUVmean, pre and post liver normalization versus response group. 29

Figure 13. SUVmax, pre and post liver normalization versus response group. 29

Figure 14. Survival analysis, splitting the groups by SUVmax and SUVmean both pre and post liver normalization. 30

Figure 15. Survival analysis using the volume obtained from the CT scan ROIs. 31

Figure 16. Correlation matrix of the volume, normalized SUVmean, and normalized SUVmax. 32

Figure 17. Comparing SUVmax between the different tumor models both before and after liver normalization. 33

Figure 18. Volume obtained from the CT contour compared to tumor model. 34

Figure 19. Survival probability of all mice following their first treatment. 35

Figure 20. Survival probability using the median risk score calculated by the Cox proportional hazards model using volume and SUVmax as the covariates. 36

Figure 21. Multiscale approach of chemoradiation resistance analysis using mouse models. 41

Acknowledgements

I extend my sincere gratitude to Kyle Lafata, Yvonne Mowery, and Ashlyn Rickard for their unwavering support and mentorship. Their guidance has been instrumental in shaping my journey as a scientist, and I am grateful for the invaluable lessons and encouragement they provided. I am fortunate to have them as lifelong mentors and friends.

I would like to express my appreciation to the Mowery Laboratory for providing me with the necessary skills and expertise crucial for the completion of this project. Their collaborative spirit and assistance with cell culturing and mouse care during my absence were integral to the success of my research endeavors.

A special thank you goes to the Lafata Laboratory for welcoming me into their research community and allowing me to contribute to their work. I am grateful for the opportunities to learn and grow within this supportive environment.

Collectively, the guidance, resources, and encouragement from these mentors and laboratories have played a pivotal role in my academic and research journey. Their contributions have significantly enriched my experience, and I am thankful for the collaborative and nurturing scientific community they have fostered.

1. Introduction and Background

1.1 Significance and Motivation

Head and neck cancers encompass malignancies affecting the tongue, oral cavity, nasal cavity/sinuses, pharynx, and larynx, with primary risk factors including tobacco use, alcohol consumption, and Human Papillomavirus (HPV) infections [1, 2]. Head and neck squamous cell carcinoma (HNSCC) manifests in the mucosal linings, predominantly in the oral cavity and larynx, with a higher prevalence in men [1, 2]. The current standard of care involves surgery and/or cisplatin-based chemoradiation therapy [1, 2]. Over the past decade, the incidence of HNSCC has seen an upward trend, with an anticipated 30% increase in incidence by 2030 [1, 2]. HPV-negative cancers exhibit genomic complexity, often presenting mutations in the TP53 tumor suppressor gene [1, 2]. Notably, HPV-negative cancers demonstrate a poorer prognosis compared to their HPV-positive counterparts, which generally exhibit greater responsiveness to chemoradiation [1]. In HPV-positive head and neck cancer cases, the risk of death is approximately 60% lower than in HPV-negative cases due to increased locoregional control, prompting discussions and trials of dose de-escalation [3, 4]. Radiation treatment for head and neck cancers can result in radiation toxicity side effects, especially to the salivary glands, resulting in decreased saliva production, dry mouth, difficulty talking and swallowing, and dental problems, all of which result in a decreased quality of life.

Identifying prognostic radiomic features on 18F-FDG micro-PET/CT images for the response to chemoradiation in mouse models of head and neck squamous cell carcinoma can contribute to the discovery of biomarkers indicative of chemoradiation resistance. This research underscores the necessity for a deeper understanding and prediction of the response spectrum of HNSCC, paving the way for more personalized care regimens for patients in the future. Dose

de-escalation can reduce radiation toxicity for patients who qualify, resulting in a higher quality of life without sacrificing treatment outcomes.

1.1.1 HPV-Positive HNSSC

HPV is a family of viruses infecting stratified epithelium and has been linked to cancers in the tissue they infect, such as the cervix and oropharynx [1, 2]. Specifically, HPV16 is the primary subtype found responsible in both cervical and oropharyngeal HPV-positive cancers [3, 2]. The discovery of the oncogenic properties of HPV infection of epithelial tissue is a relatively recent finding within the last half-century [1]. In the head and neck specifically, the tonsillar crypts are most susceptible to malignant transformation from HPV infection due to the increased expression of programmed death-1 ligand-1 (PD-L1) and an enhanced ability for the HPV to evade the immune system [1]. These tumorigenic cellular transformations can be induced as the HPV-infected cells bypass cell-cycle checkpoints by producing viral proteins that degrade tumor protein P53 and retinoblastoma protein—cancer preventative and tumor suppressor proteins—to promote viral replication through persistent infections [1].

1.2 Relevant Imaging Modalities

1.2.1 Computed Tomography Imaging

Computed tomography (CT) imaging is obtained through a rotating x-ray beam, leading to a reconstructed 3-dimensional (3D) image based on tissue attenuation, representing density in voxels using Hounsfield units (HU) [5]. These voxels, analogous to 3D pixels, reflect the average density of encompassed tissues [5]. In medicine, CT provides a valuable internal anatomical view, revealing the boundaries of tissues with varying densities [5]. However, it falls short in providing optimal contrast for soft tissues compared to magnetic resonance imaging.

Nevertheless, CT imaging remains a widely used and beneficial anatomical scan in medical practice.

1.2.2 ^{18}F-Fluorodeoxyglucose Positron Emission Tomography Imaging

Fluorine-18 (^{18}F) - Fluorodeoxyglucose (FDG) positron emission tomography (PET) imaging is a metabolic imaging modality that reveals information about cellular metabolic function [6]. Tumor cells, with an increased presence of glucose transporters and enzymes involved in glucose phosphorylation, facilitate the uptake of FDG [7]. Following phosphorylation, FDG 6-phosphate accumulates within the cell as it is not efficiently metabolized through glycolysis due to its modified structure [7]. ^{18}F serves as a positron-emitting radionuclide that interacts with an electron in the surrounding tissue, resulting in annihilation and the simultaneous release of two gamma rays in opposite directions (180° apart), subsequently detected by the scanner [8]. The reconstruction of these detections results in a 3D image pinpointing the spatial distribution of positron annihilation, indicating the internal uptake location of FDG [8]. These scans typically encompass the entire body, enabling the localization and assessment of not only the primary tumor but also nodal and distant metastases [6]. PET imaging excels at identifying smaller and submucosal lesions that anatomical scans alone, such as CT, may overlook [6]. Due to the metabolic activity information it provides, PET has become a preferred modality for monitoring treatment response in various cancers [6]. Combining PET images with coregistered CT images overlays the advantages of both scans, offering both anatomical and metabolic information.

1.2.2.1 Standardized Uptake Values, SUVmax and SUV Normalization

The units presented in the PET images are in Bq/mL; however, calibrating this reading into standardized uptake values (SUVs) accommodates variations in patient size and injected FDG dose [9].

This calibration is achieved using the formula:

$$SUV = \frac{\text{Tissue Activity (mCi/mL)}}{\text{(Injected dose (mCi)/Weight (g))}}$$

where the injected dose is time-decay corrected, and the given dose is calculated by subtracting the activity pre-injection from the residual activity in the syringe post-injection. [10]. Tumors and inflammation are likely to exhibit SUVs exceeding 2.5; however, various factors can influence SUV levels [10].

SUVmax, representing the value of the maximum SUV voxel within a region of interest (ROI), is frequently employed to evaluate activity within a lesion while excluding necrotic areas or non-malignant structures [10]. Likewise, SUVmean is the mean of all pixel intensities within the ROI, offering a more comprehensive representation of the entire region [10].

To ensure accurate evaluation, the activity detected by PET scanners from the FDG needs to be compared or normalized to the uptake in organs or structures, such as the blood pool in the heart or to the liver [11]. This comparison, facilitated by a reference organ or structure, serves as the body's background measurement [11]. One way this normalization can be achieved is by utilizing consistently placed and sized cylindrical regions of interest (ROIs) in the liver for each patient [11].

1.3 Advanced Analytical Computation Techniques in Oncology

1.3.1 Radiomics

The field of radiomics is rooted in the extraction of image features from medical imaging. In the context of oncology, one application is the prediction of clinical events using time-to-event analysis, particularly in predicting overall survival [12, 13]. The standard radiomic workflow includes ROI segmentation, image preprocessing, feature extraction, model development, and validation [12, 13].

Following image acquisition, segmentation is executed on tumors and other regions of interest. The features extracted typically encapsulate the distribution of signal intensities and spatial relationships among voxels within the designated region [12, 13]. To enhance model performance and alleviate the risks of overfitting, redundant features are excluded [12]. Determining collinearity of features can aid in feature exclusion decisions, as it may indicate variables that are highly correlated.

Radiomic features are categorized into various classes: histogram features, texture features, model-based features, transform-based features, and shape-based features [14].

1.3.1.1 Histogram Features

Histogram radiomic features describe the distribution of voxel intensity values in an image [14]. The most basic histogram statistical descriptors, known as first-order features, analyze individual voxels and characterize the overall grey-level histogram through parameters like maximums, minimums, mean, variance, and percentiles [14]. First-order histogram features in PET imaging includes SUVmean and SUVmax [14]. Advanced features can capture asymmetry in the data, such as skewness, and account for outliers affecting the distribution's deviation from a Gaussian distribution, known as kurtosis [14].

1.3.1.2 Shape-based Features

Shape-based radiomics encompass the geometric properties of regions of interest (ROIs) within an image, ranging from basic measures like volume and surface area to more intricate descriptors like compactness, sphericity, and density [14]. These can also be referred to as morphological features [15].

1.3.2 Cox Proportional Hazards Model

The Cox proportional hazards model, or Cox proportional hazards regression analysis, is an event probability analysis method that considers multiple risk factors or covariates simultaneously [16]. This analysis assesses the risk factors of a sample, their outcomes, and the time to an event, assigning a hazard ratio to each risk factor [16]. The hazard ratio (HR_n) indicates the extent to which the risk of the event occurring increases or decreases compared to the baseline probability with the addition of a risk factor (n) [16]. Applying the HR to an individual case's data yields a risk score using the provided formulas [16]:

$$\mathrm{HR_n} = e^{b_n} = \frac{\text{probability of event happening with risk factor}}{\text{probability of event happening without risk factor}}$$

$$\text{Risk Score}_i = e^{[(b_n \times X_{i,n}) + (b_{n+1} \times X_{i,n+1}) + \cdots]}$$

Here, *b* represents the regression coefficient for risk factor *n* per unit *X*, where *X* is the measured risk factor. The coefficient *b* indicates the extent to which the risk increases or decreases per unit change in *X* [16]. The Cox model is commonly implemented computationally on large datasets to calculate Cox coefficients for each covariate, allowing for the determination of hazard ratios and individual risk scores.

1.4 Relevant Clinical Background

1.4.1 Clinical Trial Investigating Prognostic Radiomic Markers in Head and Neck Cancer

In a prospective clinical trial, patients with oropharyngeal cancer undergoing chemoradiation therapy received ^{18}F-FDG PET/CT imaging both before treatment and two weeks into treatment [4]. The study aimed to assess the prognostic potential of intra-treatment PET radiomics data, focusing on the association between radiomic expression after 20 Gy and recurrence-free survival (RFS) [4]. A total of 55 radiomic features were extracted as potential biomarkers for treatment response [4]. Patients were subsequently monitored every 2-3 months for recurrence, with censoring applied on the date of the final follow-up [4]. The collected data were utilized to construct Kaplan-Meier curves for time-to-event analysis [4]. Results indicated that pre-treatment radiomics did not hold prognostic significance [4]. However, intra-treatment radiomics demonstrated prognostic value for recurrence-free survival [4].

1.4.2 Tumor Models Used in HNSSC Research

1.4.2.1 C57BL/6J Mice

C57BL/6J mice, an inbred strain, possess uniform genotypes, promoting research consistency and minimizing genomic variation [17]. These mice, characterized by a black phenotype, were originally derived in 1921 by Dr. Little and constitute the foundational Jax strain available for purchase from The Jackson Laboratory [17]. The controlled genotype of inbred mice ensures that variations in treatment response are not influenced by genetic differences between individuals. This genetic uniformity enhances the reproducibility and reliability of experimental results, enabling researchers to focus on specific treatment effects without the confounding impact of genetic variability. This attribute contributes to the consistency and validity of findings,

establishing inbred mice as a valuable model for controlled and well-defined experiments in cancer research.

1.4.2.2 MOC1 and MOC2 Cell Lines

Two mouse oral cancer (MOC) lines, MOC1 and MOC2, were developed in C57BL/6 mice through repeated exposure to carcinogens, inducing tumorigenesis [18]. Both cell lines are HPV-negative head and neck squamous cell carcinoma lines [18].

The MOC1 cell line is characterized by an indolent growth pattern, increased $CD8^+$ T-cell infiltration into the tumor microenvironment, and decreased $CD4^+$ T-cells [18]. It also exhibits inducible major histocompatibility complex (MHC) class I expression [18].

$CD8^+$ T-cells not only defend against infections but also are responsible for eliminating transformed cells [19]. $CD4^+$ T-cells, a type of T-lymphocytes, are vital for coordinating immune responses [20]. Once activated and specialized, the $CD4^+$ T-cell release specific cytokines—signaling molecules that communicate with other cells—to contribute to immune reactions [20]. They activate innate immune cells, B-lymphocytes, cytotoxic T-cells, and nonimmune cells [20]. Moreover, $CD4^+$ T-cells play a role in calming or suppressing immune reactions [20]. MHC class I molecules, present on the cell surface, bind to antigens originating from pathogens or cancerous transformations [21]. They then deliver these antigens to $CD8^+$ T-cells, signaling the $CD8^+$ T-cells to eliminate the infected cell [21].

In contrast, the MOC2 cell line is aggressive and metastatic, demonstrating decreased basal and inducible MHC class I expression [18]. It is associated with $FOXP3^+CD4^+$ regulatory T-cell infiltration and an increased presence of $CD4^+$ T-cells [18]. FoxP3 is a transcription factor that drives Treg development [18]. Additionally, MOC2 spontaneously metastasizes to draining lymph nodes [18].

Both cell lines show an increase in $CD11b^{+}/Gr1^{+}$ cells [18]. These cells play a key role in the immunotolerance of tumors [22].

1.4.2.3 MLM1 Cell Line

The recurrent and metastatic cell line derived from oropharyngeal squamous cell carcinoma, known as the Murine Lung Metastatic (MLM) cell line, is immune-competent and HPV-positive [23]. These cells were taken from a mouse that did not respond successfully to chemoradiation treatment [23]. This cell line, MLM1, expresses the parental HPV16 E6 and E7 proteins, contributing to the degradation of P53, similar to human cases of HPV-positive HNSCC [23].

2. Methods

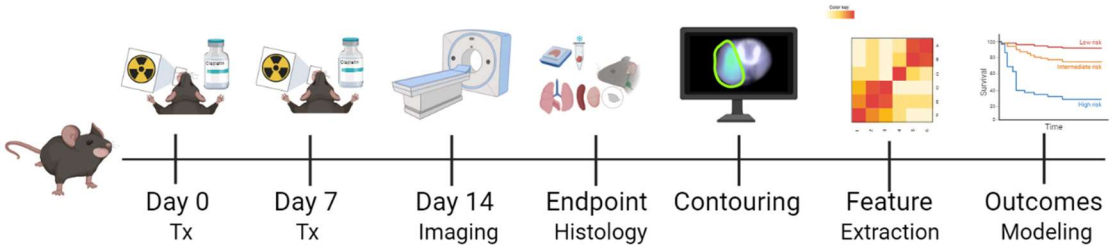

Figure 1. The experimental pipeline. Mice undergo chemoradiation treatments of 8 Gy radiation and 5mg/kg cisplatin on Days-0 and 7, followed by PET/CT imaging on Day-14. Subsequently, the acquired data is contoured, features extracted, and outcomes modeled and analyzed.

2.1 Experimental Design

All animal studies were performed in accordance with Duke University's Institutional Animal Care and Use Committee and adhere to the NIH Guide for the Care and Use of Laboratory Animals.

2.1.1 Models, Cell Culture, and Induction

2.1.1.1 Tumor Models and Cell Culture

Mouse oral carcinoma (MOC) cells lines, MOC1 and MOC2, were purchased from Kerafast, and the MLM1 (mEERL lung metastasis clone 1) cell lines were generously provided by Dr. Paola Vermeer at Sanford University. To maintain cellular integrity and prevent over confluence, all cell lines were passaged and replated every two to three days, with no more than 15 passages total prior to induction. The cells were cultured in their recommended media, details of which can be found in appendix A, and incubated at 37°C with 5% CO_2. Prior to murine injection, all cells underwent testing for murine pathogens.

In preparation for induction, culture media was aspirated, and the plate was washed with sterile phosphate-buffered saline (PBS). Then, 3 mL of trypsin (0.25% EDTA, Brand) was added to the culture plate and incubated for 7-12 minutes to release the adherent cells. The trypsin was then neutralized by washing the cells with 7 mL of fresh media and subsequently centrifuged at 300xg for 5 minutes. After cells were pelleted and the media/trypsin solution was aspirated, cells were suspended in PBS. Subsequently, a 20 µL aliquot of cell solution was combined with 20 µL of Trypan blue (brand) to mark nonviable cells with a compromised cellular membrane. Then 10 µL of this mixture was added to a hematocytometer for the enumeration of viable cells. Based on this information, the cell mixture was appropriately diluted with either 1:1 PBS:Matrigel (Corning) or PBS alone.

For the MOC1 and MLM1 cell lines, 300,000 cells/50 µL were injected per mouse, resuspended in a 1:1 PBS and Matrigel solution. In the case of MOC2, 30,000 cells/50 µL were resuspended in PBS alone.

2.1.1.2 Induction

127 C57BL/6J mice (Jackson Laboratories), both male and female, were purchased at 6 weeks of age and induced between 6 and 10 weeks of age. For orthotopic buccal tumor inductions, mice were anesthetized under <3.5% isoflurane (with 100% oxygen carrier gas). Using forceps, the mouse's upper lip was grasped, and the needle tip was inserted into the right buccal oral mucosal where the bolus of tumor cells was delivered. Any leakage during the injection was noted and removed, and the mice were supervised until recovered on a 37°C heated pad.

2.1.2 Monitoring the Mice

Following induction, all mice were monitored and assessed for the development of tumors at least three times per week. In the presence of any observed asymmetry, digital calipers measured the tumor in two dimensions (Figure 2), and the tumor volume was approximated as a cylinder:

$$V_{Tumor} = \frac{\pi}{6} length \times width^2$$

where *length* is the longest dimension of the tumor and *width* is the dimension perpendicular to the *length*.

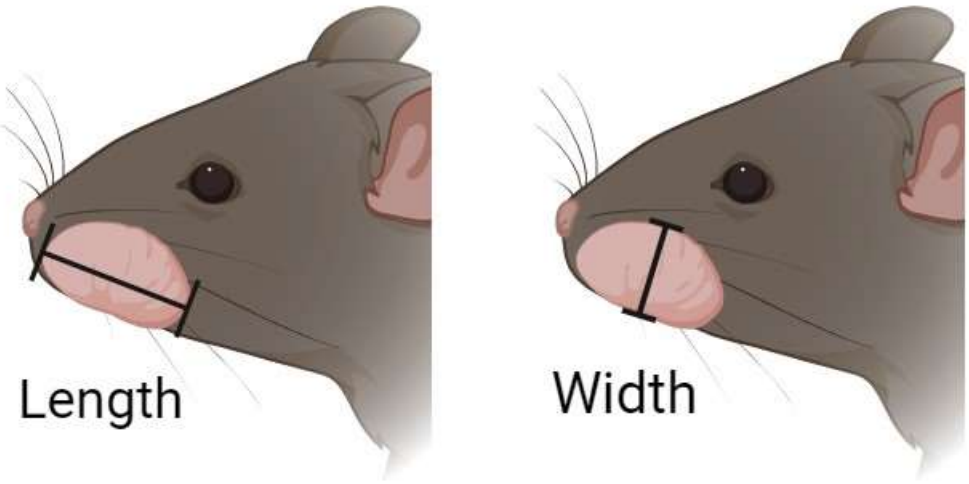

Figure 2. Dimensions measured externally using calipers to allow for a cylindrical volume approximation.

Upon exceeding the cylindrical volume threshold of 50 mm^3, treatment was initiated.

During the thrice-weekly monitoring sessions, any mouse requiring supportive care received appropriate interventions including a 0.5 mL subcutaneous saline bolus, softened food, and peanut butter.

2.1.3 Chemoradiation Treatment

Mice were treated concurrently with two fractions of 8 Gy radiation and cisplatin, administered one week apart, with the 16 Gy over two weeks being the mouse biological equivalent dose to the 20 Gy in the human clinical study conducted by Lafata et al. On Day 0 and Day 7, at least 30 min prior to radiation, 5 mg/kg cisplatin was administered intraperitoneally. Mice were irradiated on the Xstrahl Small Animal Radiation Research Platform (SARRP), (225 kV & 13 mA). Two opposed lateral beams were used per treatment (4 Gy each). Prior to each irradiation, setup was confirmed via on board fluoroscopy. During treatment, mice were anesthetized via 2% isoflurane with a 100% O_2 carrier. The mice then recovered on a 37°C heated pad. In the two days following each chemoradiation treatment fraction, the mice were administered 0.5 mL of subcutaneous saline to prevent nephrotoxicity.

2.1.4 ^{18}F FDG PET/CT Imaging

The ^{18}F FDG PET/CT images of the mice were obtained on Day 14, one week after their second chemoradiation treatment. Twenty-four hours prior to imaging, the mice were fasted with access to water alone. On the day of imaging, ^{18}F FDG was administered via tail vein injection and allowed 60 minutes for uptake. Subsequently, the mice were imaged on a microPET/CT Siemens Inveon scanner under isoflurane anesthesia.

2.1.5 Humane Endpoints

Once the tumor measured greater than 12mm in any dimension, the tumors were ulcerated, or mice lost more than 25% of their initial body weight, they were humanely

euthanized, and necropsies were conducted. Oral tumors, cervical lymph nodes, lungs, and spleens were collected, which were then placed into blocks for formalin fixation (10% formalin for 24 h then placed in 70% EtOH) and paraffin embedding (FFPE). The lungs were inflated with 10% formalin during this process. A portion of the tumor was excised and promptly flash-frozen using liquid nitrogen, then stored at -80°C for subsequent immunohistochemical analyses.

2.2 Data Analysis

2.2.1 Tumor Model Growth, Response, and Survival Analysis

To assess survival, the number of days the mouse survived beyond the first treatment fraction were recorded. Any mouse who passed due to reasons unrelated to the cancer process, such as those who passed during the PET/CT imaging process, were censored. Additionally, those mice who survived beyond the observation period of 200 days were also censored. The data was compiled in a Kaplan-Meier graph and a Log-Rank test was used to determine significant differences amongst models. A p-value of < 0.05 was considered significant, and all survival statistical analyses were performed in MATLAB.

Applying the cylindrical volume approximation, the volumes obtained thrice weekly were normalized to the volume on the initial day of treatment. This normalization was essential to account for variations in the first volume surpassing the treatment threshold among individual mice. Utilizing survival data, the median survival time was determined for each model. The smallest median survival time, 31 days, served as the criterion for assessing growth and response.

Mice were categorized into responders and non-responders for the subsequent response analysis. A responder was defined as a mouse whose normalized tumor volume on day 10 of treatment was less than 1, indicating tumor shrinkage following the two fractions of chemoradiation. Additionally, exceptional responders were defined as any mouse who at any

point during the monitoring period had an external tumor volume recorded as $0mm^3$ (no visible asymmetry to measure with calipers). Significant differences in growth trends amongst models and response groups were determined using ANOVA and group-wise Tukey's post-test, with a p-value of <0.05 being considered significant. The growth statistical analyses were performed in GraphPad Prism.

2.2.2 Image Feature Analysis

2.2.2.1 Segmentation of Tumor and Liver Regions of Interest and Image Feature Extraction

The PET/CT images were imported into the Gremse-IT Imalytics Preclinical software and blinded to tumor model. To contour the tumors, initial regions of interest (ROIs) were drawn based on asymmetry and anatomy within the CT images. Subsequently, these initial ROIs underwent further segmentation using Hounsfield units (HU) thresholding, considering only the regions with HU values falling within the range of 75-300, with this range selected due to literature review (see Table 1) and results approved by a radiation oncologist. Following this, a Gaussian filter (standard deviation of 2.0) was applied to the binary mask of the selected class. The binary mask was then reverted. For quality control, a random sampling of 40% of the contours were reviewed by a Radiation Oncologist with manual adjustments made as necessary.

Table 1. Reference Hounsfield units and resultant thresholding range selected for the ROI segmentation process.

Tissue	Hounsfield Unit Range	Source
HNSCC	50 to 330 HU	Forghani, et al. 2015
Soft Tissue, Mouse	-100 to 200 HU	Yep, et al. 2004
Fat	-150 to 50 HU	Kim, et al. 1999
Bone	300 to 3000 HU	Schreiber, et al. 2011
Selected ROI Thresholding Range	**75 to 300 HU**	

Following the tumor contouring, three cylindrical samples of the liver, each with a diameter and length of 1 mm, were contoured as a new class for subsequent SUV normalization.

The PET images underwent calibration to standard uptake values (SUV) for subsequent analysis, using metadata extracted from the PET DICOM files. The contoured volume, SUVmax, and SUVmean values for both classes – the tumor ROIs and the liver samples – were compiled. These values were then tabulated alongside survival and growth data for further analysis. Additionally, SUVmax and mean values were normalized to the liver SUVmean.

To assess the correlation between external caliper measurements and cylindrical volume approximation, volume measurements obtained from contoured regions were compared with those taken on the imaging day or the nearest available date. These values were plotted, and a linear fit was applied for evaluation.

2.2.2.2 Univariate Response Analysis

Treatment response was analyzed univariately and blinded to the tumor model concerning the volume obtained from the tumor region of interest, as well as SUVmax and

SUVmean, both before and after normalization to the liver SUVmean. For image analyses, mid- and high-responders were combined into a single response group and compared to the low-responders. The normality of the data was assessed using the Lilliefors test with a threshold significance level of 0.05. Subsequently, the data were subjected to either the t-test or Mann-Whitney U test, depending on the distribution. The specific statistical tests employed to assess response with each covariate can be found in Table 2. For all tests, a p-value < 0.05 was considered significant.

Table 2. Covariates analyzed in the univariate response analysis and corresponding statistical test employed.

Covariate	Statistical Test
Volume	Mann-Whitney U test
SUVmax	Mann-Whitney U test
SUVmax, normalized to liver	Mann-Whitney U test
SUVmean	t-test
SUVmean, normalized to liver	Mann-Whitney U test

2.2.2.3 Univariate Survival Analysis

SUVmax and SUVmean, both before and after normalization to the liver, and the volume from the contoured tumor ROI, underwent univariate analysis blinded to the tumor model concerning survival. The stratification was based on the median value of the covariate under examination. The data were visually represented through a Kaplan-Meier plot and assessed using the log-rank test, with statistical significance set at a p-value < 0.05.

2.2.2.4 Univariate Image Features and Tumor Model Analyses

Collinearity of features were assessed to determine inclusion/exclusion from the multivariate analysis. Correlation coefficients were calculated using MATLAB for post liver-normalization SUVmean, SUVmax, and volume.

Image features were examined in relation to the tumor model to ensure that there was enough variation in SUVmax and tumor volumes across the models. This enabled the evaluation of whether either of these features could function as proxies for the tumor model. The data were assessed for normality using the Lilliefors test before statistical analysis to ensure the selection of the correct test. Differences between the tumor models and SUVmax, both pre and post normalization to the liver, were analyzed in MATLAB using Kruskal-Wallis and post hoc Tukey's tests. Differences between the tumor models and volume were examined with ANOVA and post hoc Tukey's test. For all tests, a p-value < 0.05 was considered significant.

Each mouse had coefficients of variation (CV) determined for liver SUV values within the liver ROIs to verify the uniformity of SUV distribution within the liver ROIs. CVs were calculated using the following formula:

$$CV = \frac{\sigma}{\mu}$$

Maximum, minimum, and mean CV for all samples were determined.

2.2.2.5 Multivariate Survival Analysis

Normalized SUVmax, volume, and survival duration were fed into the Cox proportional hazards model on MATLAB and regression coefficients (b) for SUVmax and volume were computed. Hazard ratios for the n^{th} covariate can then be calculated as follows:

$$HR_n = e^{b_n}$$

Subsequently, risk scores for each mouse were computed using the following formula:

$$\text{Risk Score}_i = e^{[(b_{\text{SUVmax}} \times \text{SUVmax}_i) + (b_{\text{volume}} \times \text{Volume}_i)]}$$

where *i* is the individual mouse. The risk scores were then divided using the median into two groups: high risk and low risk. These groups were plotted using a Kaplan-Meier plot and assessed for significance using the log-rank test. A p-value < 0.05 was considered significant.

3. Results

The experiment was successfully completed with the treatment, imaging, and analysis of 121 mice. However, 2 mice were excluded from the image analysis as their tumors were cured prior to the imaging process, and an additional 4 were excluded from certain analyses due to insufficient metadata in the DICOM files, which resulted in a failure to complete SUV calibration.

3.1 Tumor Model Growth, Response, and Survival Analysis

When examining the growth trends among the three models, significant differences in their growth patterns were identified, as illustrated in Figure 3 (MLM-MOC2 $p \leq 0.01$, MLM1-MOC1 and MOC1-MOC2 $p \leq 0.0001$, ANOVA, Tukey's post hoc analysis). Error bars represent the standard deviation.

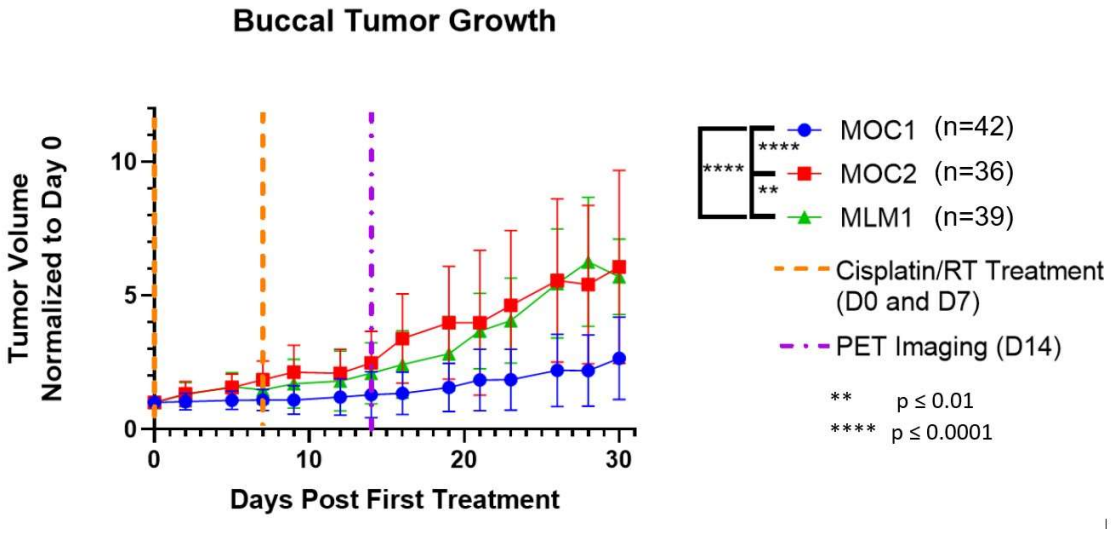

Figure 3. Tumor growth trends using normalized tumor volume post first treatment: comparison of the three tumor models.

Additionally, all three models displayed significant differences in their survival, as seen in Figure 4 ($p = 1.76e-09$, log-rank, MLM1-MOC1 ≤ 0.05, MLM1-MOC2 and MOC1-MOC2 $p \leq 0.0001$, pairwise log-rank.)

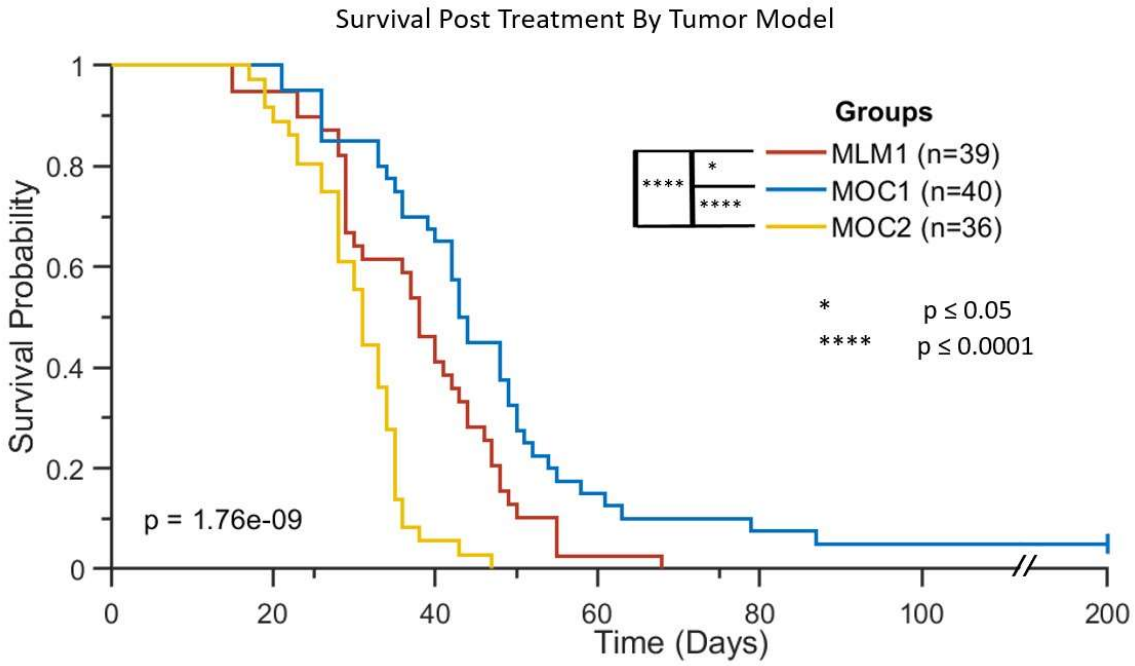

Figure 4. Survival probability post treatment based on tumor model.

Median survival time also varied between models (Table 3).

Table 3. Median survival time based on tumor model.

Tumor Model	Median Survival (days)
MOC1	43
MOC2	31
MLM1	38

Using day 10 post initial treatment as the threshold for response resulted in significant growth trend differences between response groups when divided between responders (high- and mid- combined) and low-responders (Figure 5) ($p \leq 0.0001$, ANOVA). When separated into high-, mid- and low-responders, all three response groups displayed significant differences in growth trends (Figure 6) ($p \leq 0.0001$, ANOVA, Tukey's post hoc). Error bars on both figures show the standard deviation.

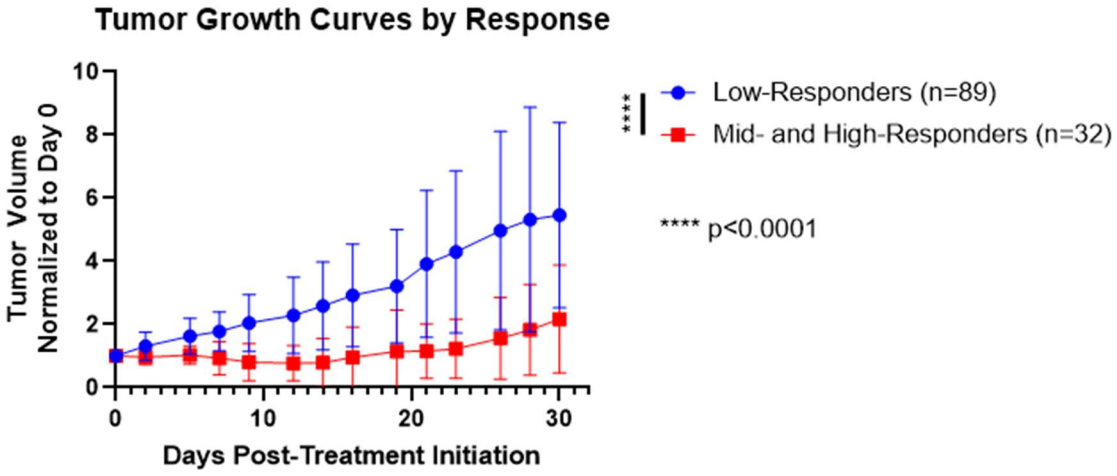

Figure 5. Normalized tumor growth based on treatment response. Response was determined on Day 10, with low-responders being those whose normalized tumor volume was >1.

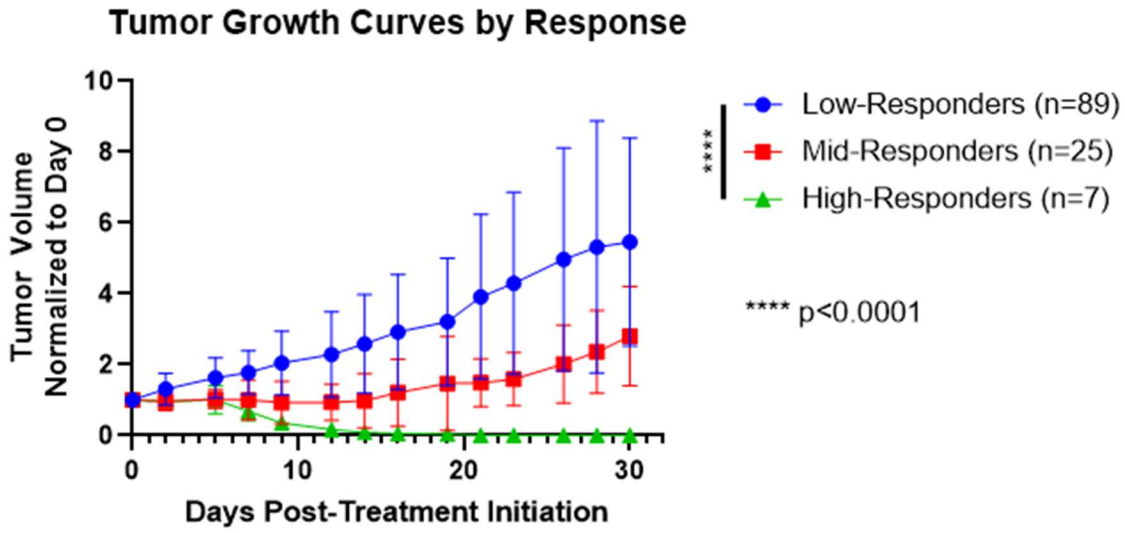

Figure 6. Tumor growth based on response showing high-, mid-, and low-responders. High-responders were any mouse whose tumor volume = 0 at any point post initial treatment.

Comparing response back to tumor models, the distribution of response within each model is displayed in Figure 7.

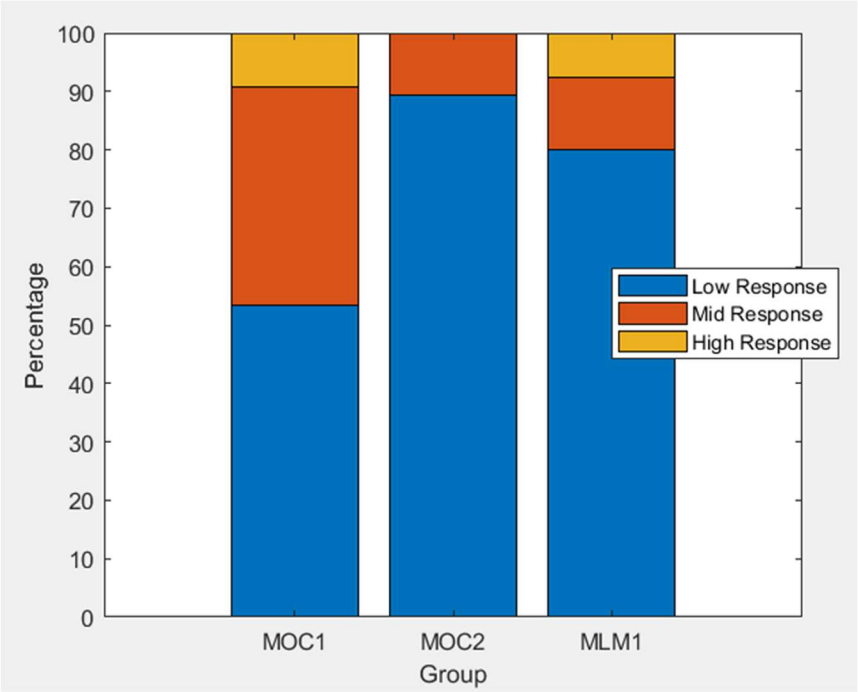

Figure 7. Distribution of response within each tumor model. High-responders were any mice whose externally measured tumor volume = 0 at any point during the observation period, mid-responders were mice whose tumor volume on day 10 normalized to the size of their first treatment was less than or equal to 1, and low-responders were any mice whose normalized day 10 tumor volume was greater than the volume in which they initiated treatment.

3.2 Image Feature Analysis

3.2.1 Segmentation Results

Figure 8 illustrates a complete segmentation in axial view, depicting the tumor region of interest in red, with snapshots captured every 2 CT slices. Additionally, Figure 9 shows a closer view of slice 119 from Figure 8 with basic anatomy labeled.

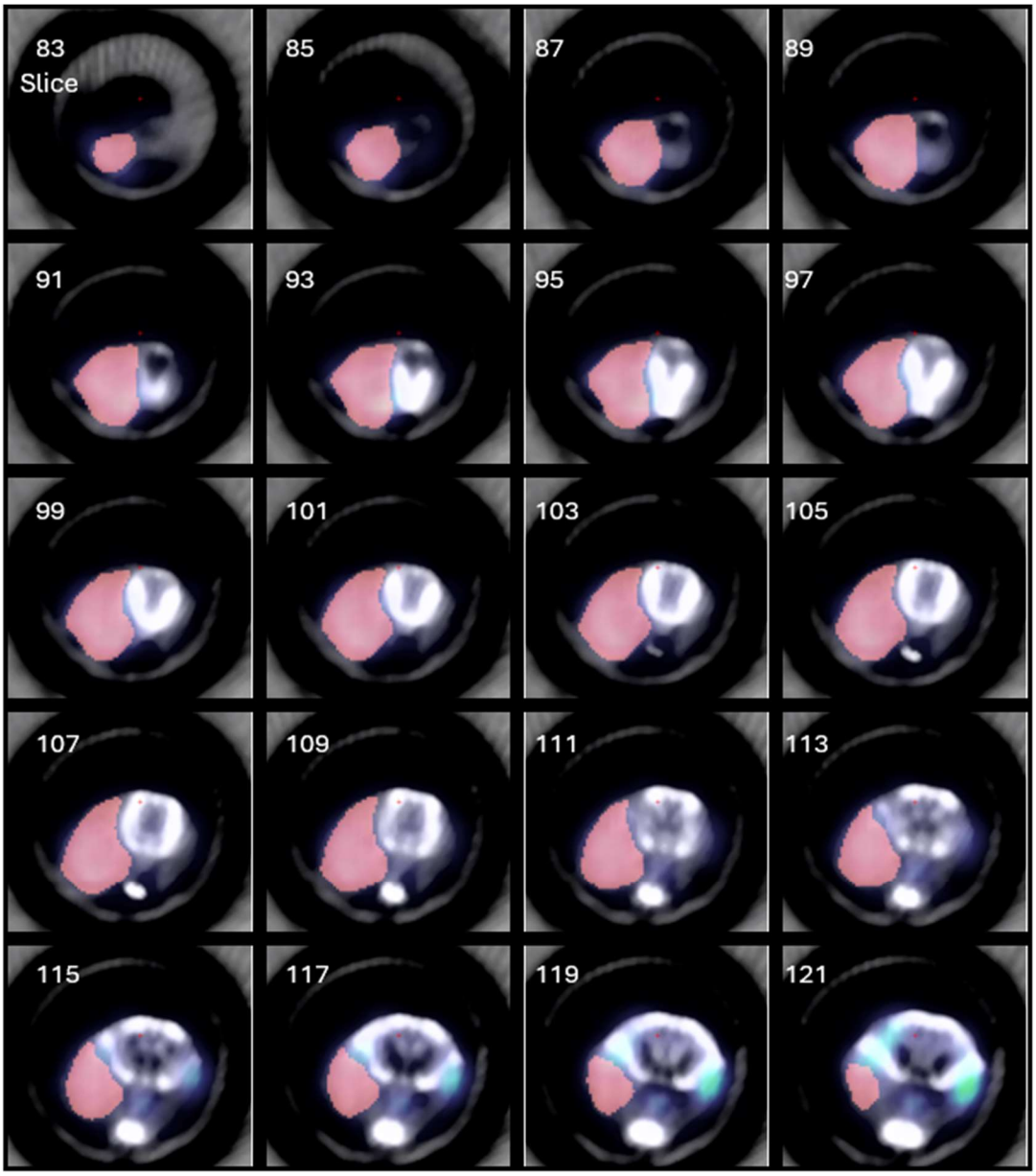

Figure 8. Example segmentation result. The contoured tumor region of interest is shown in red overlaying the axial PET/CT images, with screen captures taken every 2 slices. The number in the top corner represents the slice number.

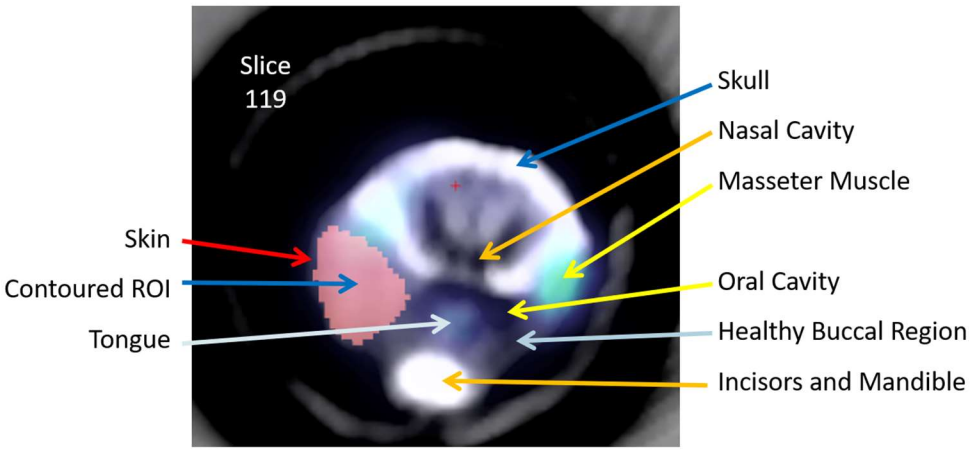

Figure 9. Example PET/CT slice with anatomy labeled.

Some descriptive statistics regarding the image feature data extracted from the entire dataset can be found in Table 4.

Table 4. Descriptive statistics regarding image features extracted from the PET/CT contoured regions of interest in the tumor and liver, rounded to two decimals, for the complete dataset.

	Volume (mm^3)	Tumor SUVmax	Tumor SUVmean	Liver SUVmax	Liver SUVmean	Normalized SUVmax
Mean	110.83	4.13	2.17	0.81	0.57	7.67
Median	93.71	3.70	2.09	0.82	0.58	6.68
Minimum	11.53	0.14	0.07	0.05	0.04	2.56
Maximum	400.51	10.50	4.24	1.42	1.10	31.74

Comparing the external caliper measurement cylindrical volume approximation obtained on the day closest to the imaging day or on the imaging day itself to the volume obtained from the contour on the imaging day resulted in a linear fit with an R^2 value of 0.7821 (Figure 10). The slope of the linear fit line is 0.7221.

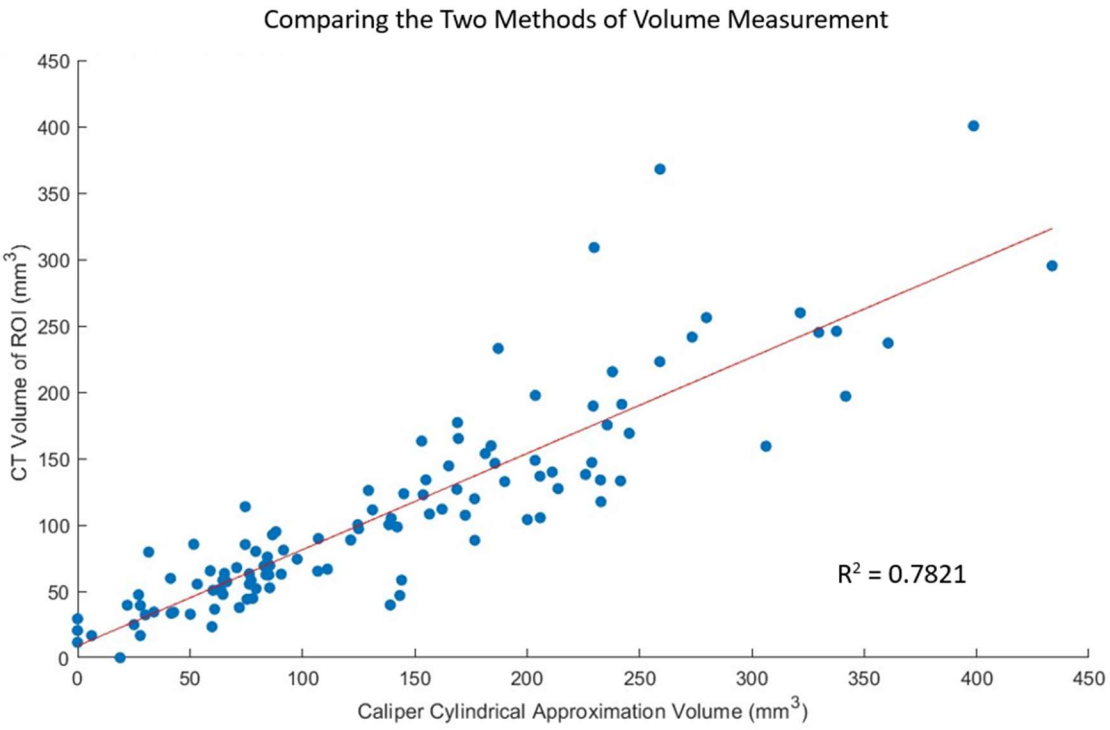

Figure 10. Comparing the results of the two volume measurement methods on the same or closest neighboring days. One was acquired via the ROI contoured on the CT scan and the other using digital calipers and the cylindrical volume approximation method. The slope of the linearly fit trend line is 0.7221.

3.2.2 Univariate Response Analysis

Using the volume obtained from the CT contours and analyzing them based on the low- versus mid-/high-responders, it was found that the volume of the tumor on day 14 was significantly related to response, as shown in Figure 11 (p = 7.0313e-9, Mann-Whitney U test).

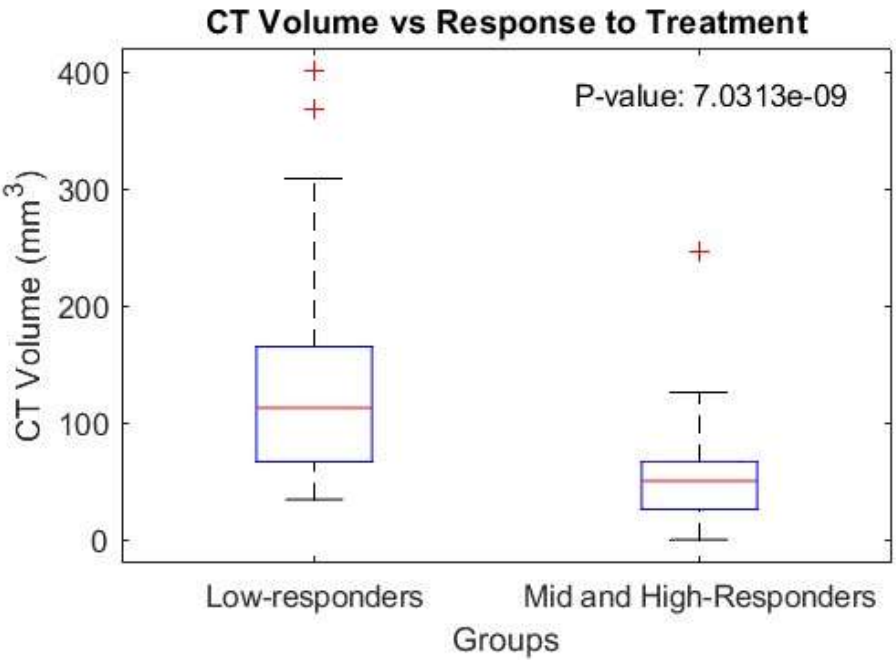

Figure 11. Volume of segmented ROIs on the PET/CT scans versus treatment response group.

However, looking at the SUVmean between the two response groups, both pre- and post-normalization to liver mean, resulted in insignificant differences (Figure 12) (pre-normalization $p = 0.3664$, t-test, post-normalization $p = 0.3487$ Mann-Whitney U test). However, significant differences were seen when comparing SUVmax pre- and post-normalization to the response groups (Figure 13) (pre-normalization $p = 0.0202$, post-normalization $p = 0.006751$, Mann-Whitney U test).

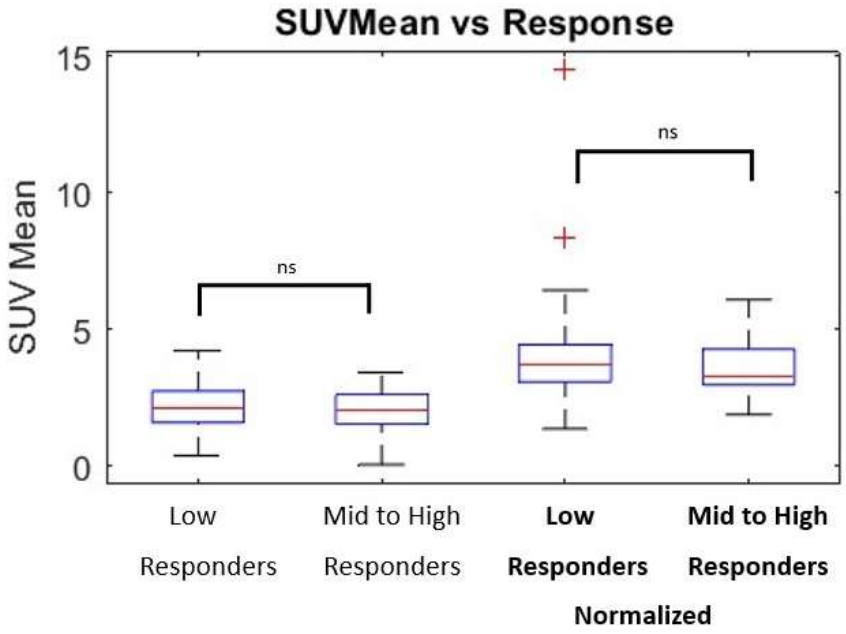

Figure 12. SUVmean, pre and post liver normalization versus response group.

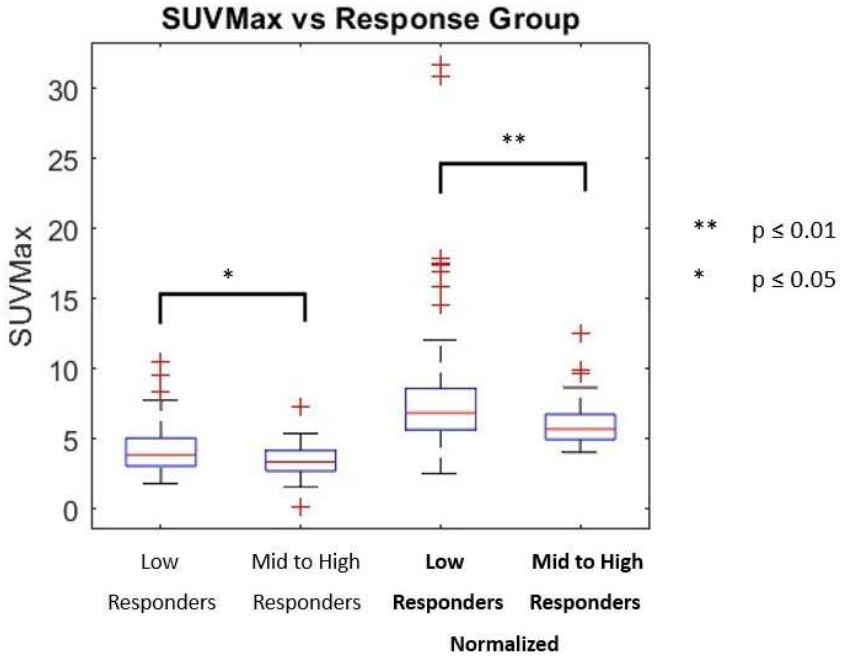

Figure 13. SUVmax, pre and post liver normalization versus response group.

3.2.3 Univariate Survival Analysis

Looking at survival compared to both SUVmean and SUVmax pre- and post-normalization, when segregated by the median, all resulted in significant differences as seen in Figure 14.

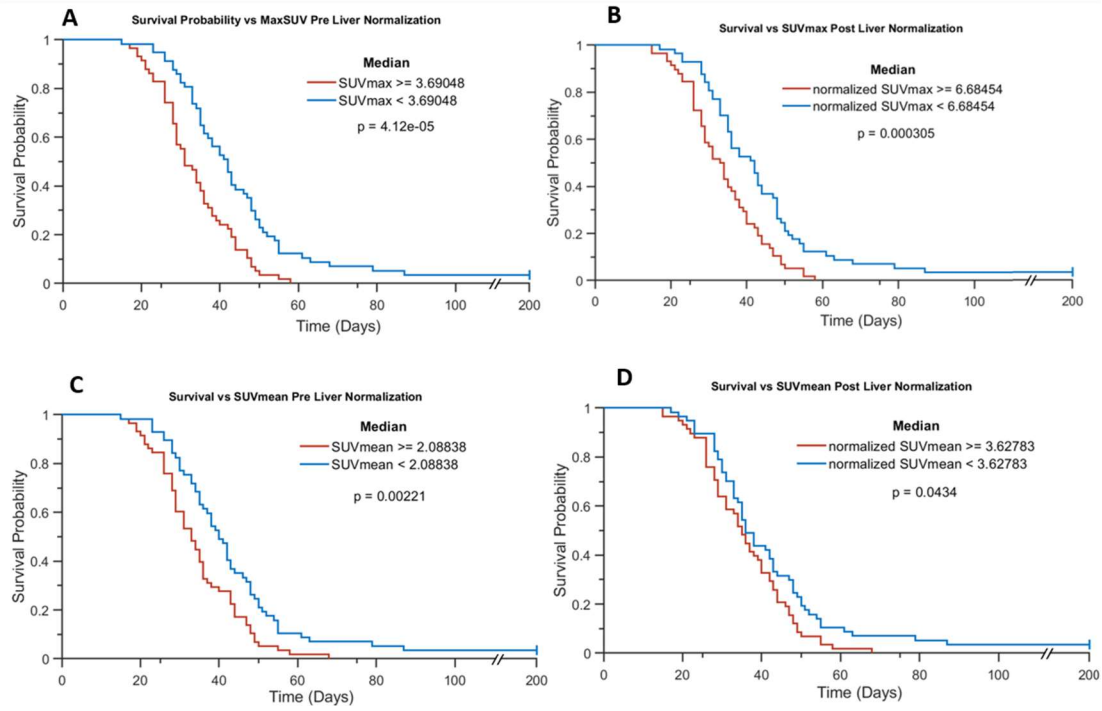

Figure 14. Survival analysis, splitting the groups by SUVmax and SUVmean both pre and post liver normalization. A) Groups divided using median SUVmax before liver normalization. B) Groups divided using median SUVmax after liver normalization. C) Groups divided using median SUVmean before liver normalization. D) Groups divided using median SUVmean after liver normalization.

Using the median volume from the ROI segmentations, the difference between survival durations post treatment has the smallest p value, where p = 2.18e-20 (log-rank) (Figure 15). The median survival time for those with a volume above the median was 29 days, compared to a 47-day median survival time for those with a volume below the median.

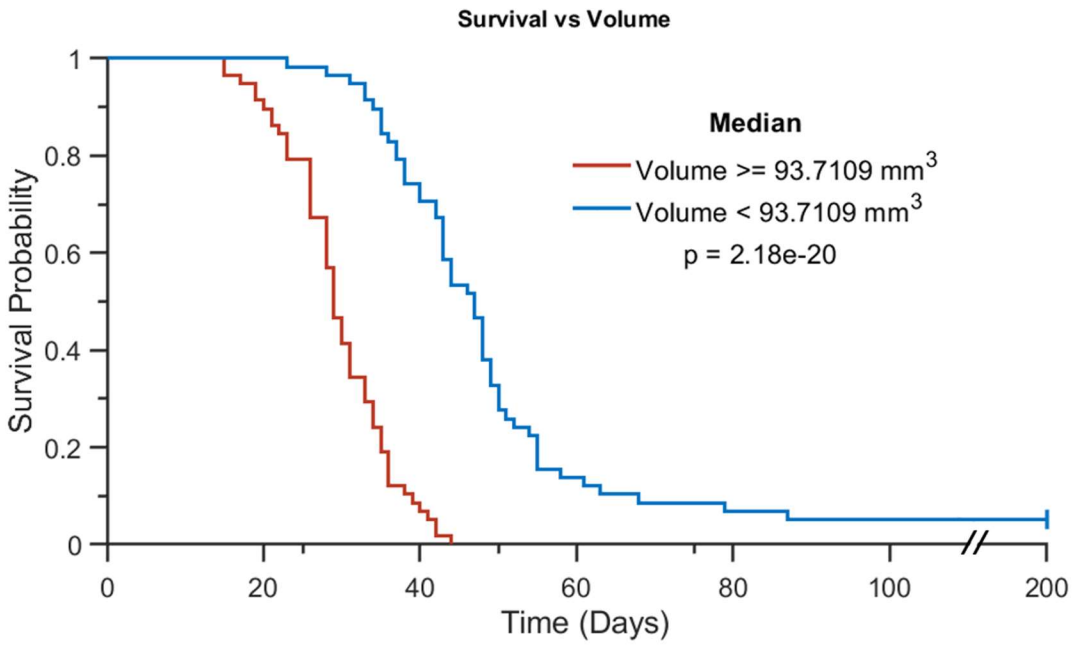

Figure 15. Survival analysis using the volume obtained from the CT scan ROIs.

3.2.4 Univariate Image Features and Tumor Model Analyses

Collinearity among image features were assessed using a correlation matrix, and the results are illustrated in Figure 16, resulting in the exclusion of SUVmean from further analyses.

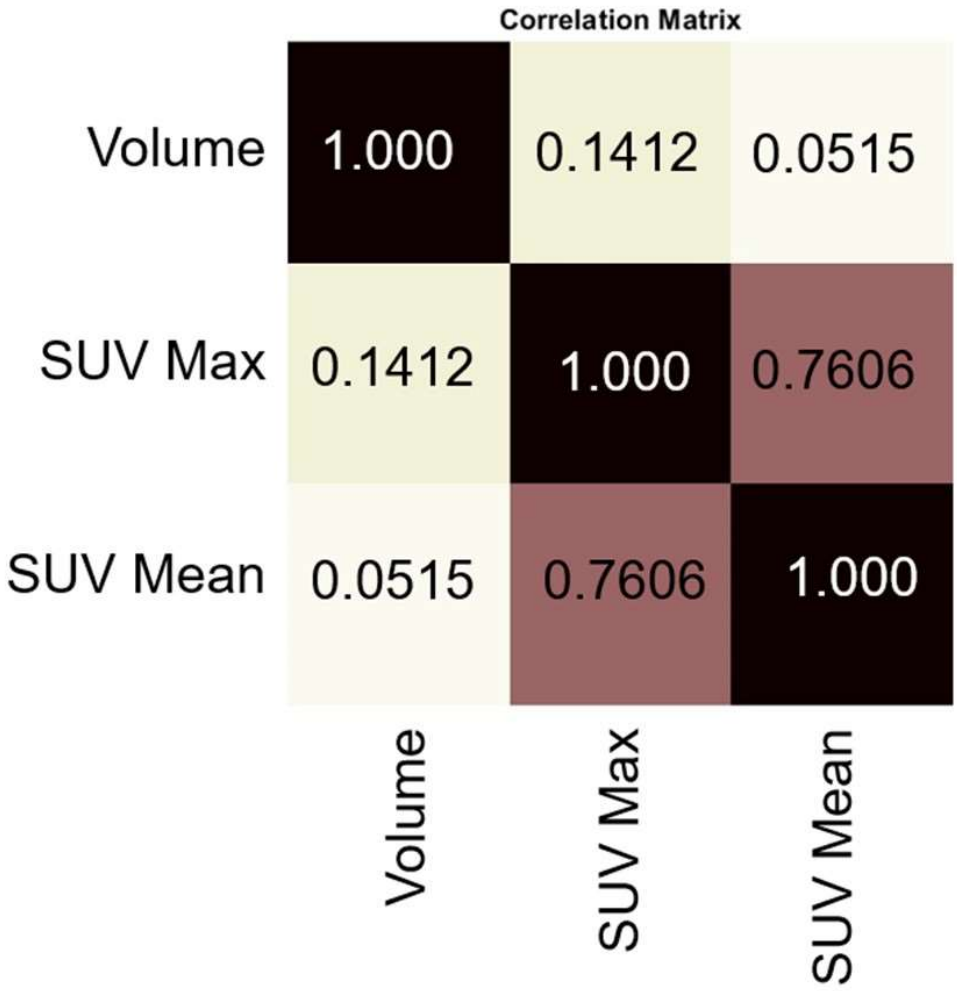

Figure 16. Correlation matrix of the volume, normalized SUVmean, and normalized SUVmax.

SUVmax was compared across tumor models both pre- and post-normalization to the liver. The results show no significant differences in SUVmax amongst tumor models (Figure 17) (Kruskal-Wallis, post hoc Tukey's test).

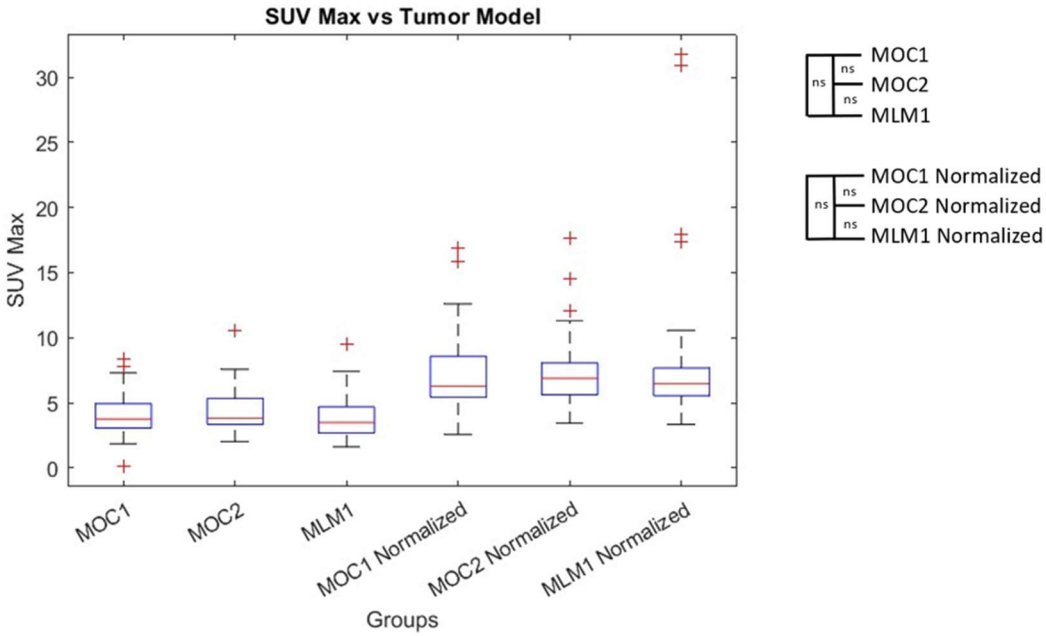

Figure 17. Comparing SUVmax between the different tumor models both before and after liver normalization. The results show the differences between the models to be insignificant.

The volume obtained using the CT segmentations was also compared against tumor model, with the only significant difference being between the MOC1 and MOC2 tumor groups (Figure 18) ($p = 0.0138$, ANOVA, post hoc Tukey's test).

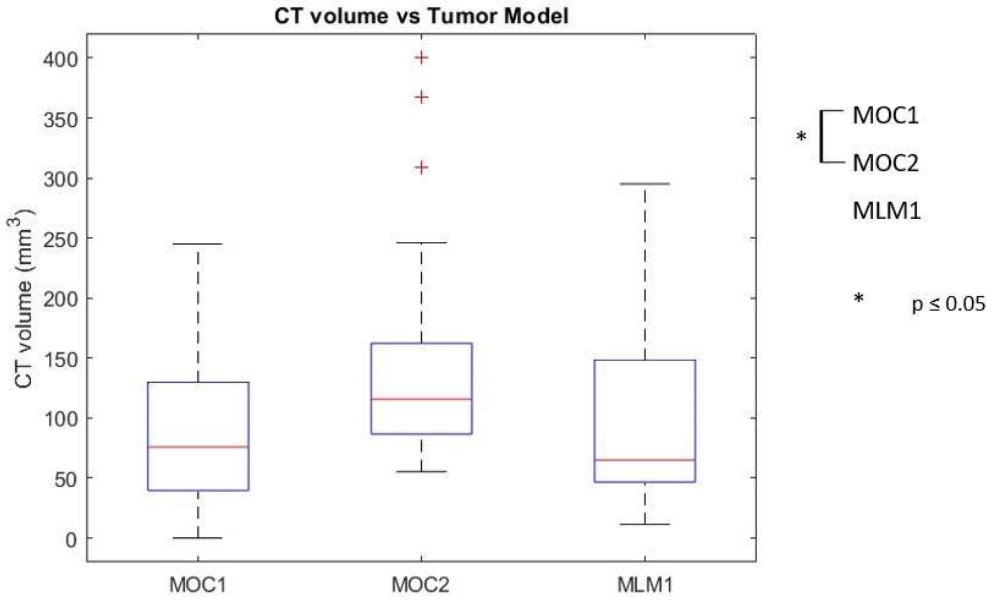

Figure 18. Volume obtained from the CT contour compared to tumor model.

Statistical information regarding the Coefficient of Variation (CV) for all liver segmentations regarding SUV measurements can be found in Table 5.

Table 5. Statistical parameters analyzing the coefficients of variation for all liver segmentation SUV measurements.

Parameter	Value
Mean CV	0.167
Maximum CV	0.354
Minimum CV	0.029

3.2.5 Multivariate Survival Analysis - Cox Proportional Hazards Model

The survival duration probability of all 115 mice can be seen in Figure 19.

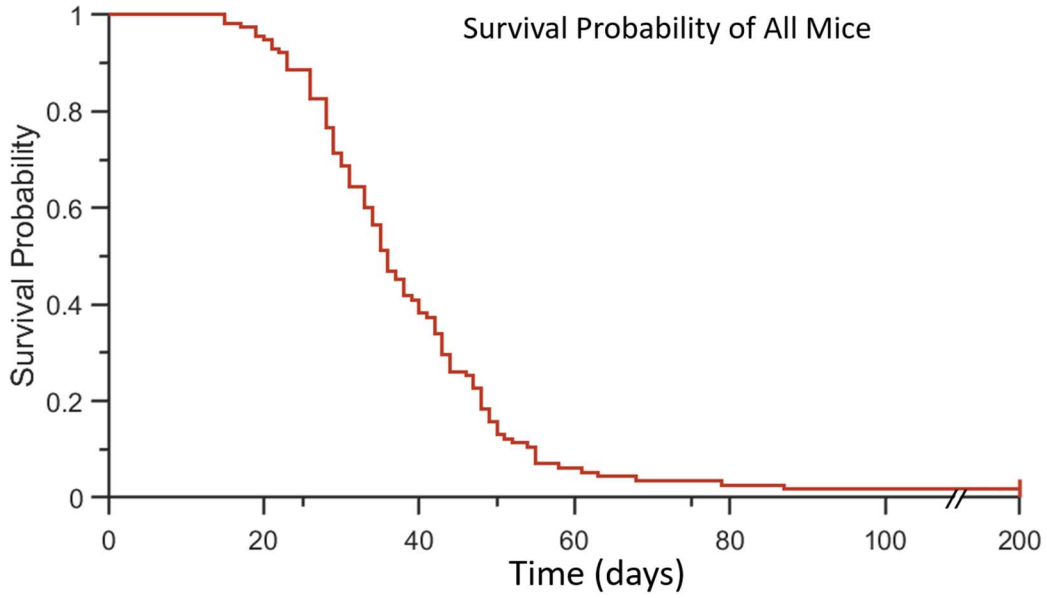

Figure 19. Survival probability of all mice following their first treatment.

The resulting coefficients and hazard ratios calculated using the Cox proportional hazards model can be found in Table 6.

Table 6. Cox proportional hazards model coefficients for covariates and resultant hazard ratios.

Covariate	Cox Coefficient	Hazard Ratio
SUVmax	0.0524	1.0538
Volume	0.0150	1.0151

Applying the coefficients from Table 6 to calculate the risk score for each case resulted in the Kaplan-Meier curve shown in Figure 20, segmented using the median risk score (p = 2.22e-20, log-rank).

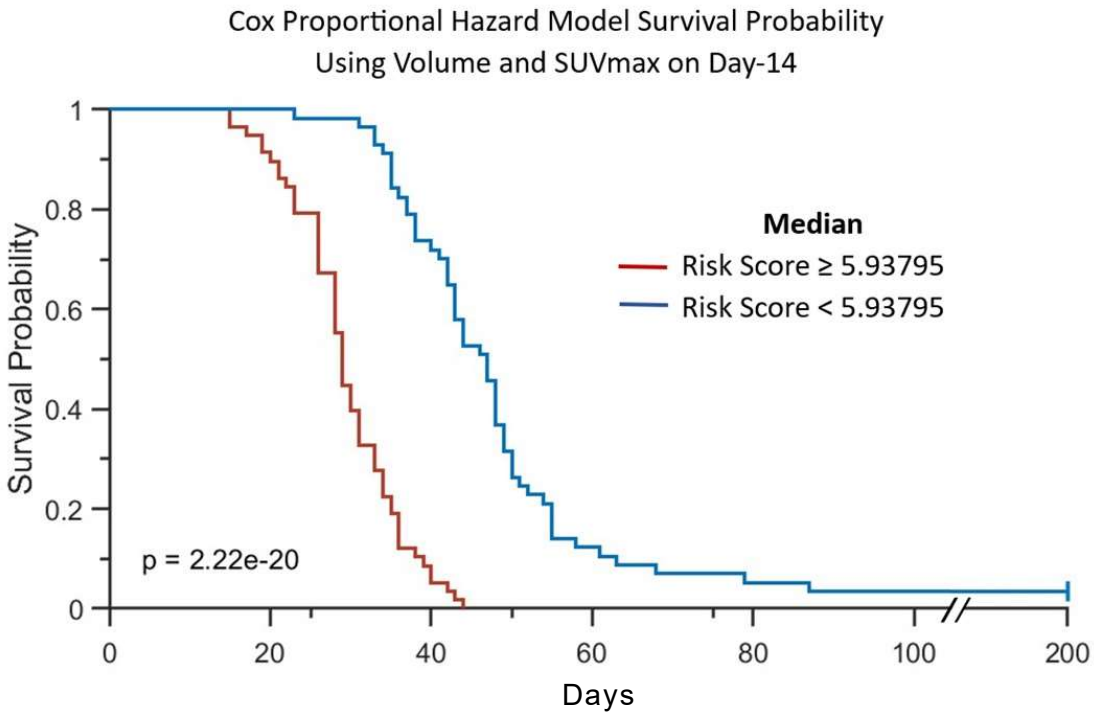

Figure 20. Survival probability using the median risk score calculated by the Cox proportional hazards model using volume and SUVmax as the covariates.

4. Discussion

4.1 Tumor Model Growth, Response, and Survival

The observed variations in growth rates among models contribute to the diversity of responses within the dataset. This diversity is further reflected in significant differences in overall survival outcomes among the models. MOC1 mice exhibit a significantly greater median survival duration and a delayed growth pattern compared to MOC2 mice, consistent with the literature [18]. Additionally, each model exhibits a substantial range of growth rates as indicated by the error bars denoting standard deviation. The presence of diverse responses, both between and within models, within a large sample size, enhances the robustness of the data pool for subsequent imaging biomarker analysis.

Analyzing the 30-day growth trends, day 10, which occurred three days post the mice's second treatment fraction, was deemed an appropriate time point for evaluating treatment response. This significance is emphasized by notable disparities in both growth patterns and survival outcomes between mid- to high- and low-responding groups. Furthermore, the significant differences in growth patterns between response groups supports the decision of defining response based on whether day 10 volume changes compared to the volume on the day of treatment initiation were positive or negative.

4.2 Image Feature Analysis

4.2.1 Segmentation Results

After considering various methods for standardizing and systematically segmenting this extensive sample size, this Hounsfield unit thresholding method was chosen. The threshold range of 75-300 HU was selected based on both a literature review and case-specific observations. Many mice showed a noticeable drop in Hounsfield Units from the 70-100 HU range to a

negative value within a few pixels, aligning with expected skin thickness and Hounsfield unit analysis [24, 25, 26]. Additional spot check analyses to verify consistency across mice included measurement of tissue thickness being excluded from the external border of the contoured region using this thresholding range, which remained consistent across mice. Based on the literature, the range of mouse skin thickness ranges from 0.204-0.280mm [24]. Furthermore, the CT scans' voxel size and resultant contour pixel size is 0.210 mm in all three dimensions, facilitating an additional visual spot check for the approximate measurement of excluded tissue.

Growth and response analysis relied on accurately observing volumetric changes using external caliper measurements. Understanding how these volume approximations were compared to volumetric measurements taken using CT contours was important. When comparing the volume derived from the contoured CT scans to the approximated volumes on either the imaging day or the nearest available date with data, the reasonable linear fit with an R^2 value of 0.7821 is notable. Additionally, the slope of the linear fit being less than 1 suggests that the volumetric approximation tends to overpredict the contoured tumor volume. A source of error includes tumors taking irregular shapes rather than a cylindrical form. Moreover, as most mice underwent PET imaging in the morning and were not accessible in the housing facility for same-day measurements due to radiation dose safety precautions, many of the volumetric comparisons were made with nearest date measurements rather than consistently same-day measurements. For mice with rapidly growing tumors, a significant change in volume within a single day would likely occur. However, for mice with imaging in the afternoon, caliper measurements on the imaging day were feasible due to access before FDG administration.

4.2.2 Univariate Response and Survival Analysis

While both response and volume were derived from volumetric measurements, they employed different methods of comparison (inter- versus intra-mouse). Response concentrated on

the volume change within an individual mouse, utilizing an intra-mouse analysis with volumes normalized to the individual on the day of initial treatment. This normalization considered variations in volume on the initiation day, as treatment initiation occurred when the threshold of 50 mm^3 was surpassed, resulting in initial volumes across mice to be nonuniform. Conversely, volume analyses using the contoured volume entailed an inter-mouse comparison, comparing raw volumes in mm^3 on equivalent days across the sample.

Volume obtained from the CT contours served as a key predictor for both response and overall survival. Mice in the mid- to high- responding groups exhibited significantly smaller volumes compared to the low- responding group, albeit with some overlap between the two groups. Furthermore, upon dividing the mice into two groups based on the median volume (93.7109 mm^3), a notable difference in overall survival trends emerged, with the group above the volumetric median exhibiting a shorter median survival (29 days) compared to those below the volumetric median (47 days). This aligns with the humane endpoints chosen, where tumor dimension served as a humane endpoint, indicating that mice with larger tumors on imaging day were more likely to be euthanized sooner.

Moreover, when survival was analyzed using the median value of SUVmax, mice above the SUVmax median—indicating higher metabolic activity —exhibited a decreased overall survival probability. Additionally, mid- to high-responding mice showed a significantly lower SUVmax, indicating decreased metabolic activity within the tumor. This is consistent with literature, where more metabolically active tumors have a poorer prognosis [27].

4.2.3 Univariate Image Features and Tumor Model Analyses

The collinearity assessment produced correlation coefficients regarding the relationship between SUVmax, SUVmean, and volume. Any correlation coefficient above a threshold of 0.5 was considered strongly correlated, leading to the exclusion of one parameter from the

multivariate model. SUVmean and SUVmax exhibited a correlation coefficient exceeding this threshold. Considering the analysis of SUVmax as a significant factor in response prediction and SUVmean being insignificant, the use of SUVmax as a covariate in the clinical study, as well as a greater separation in the Kaplan Meier survival curves when comparing median SUVmax versus median SUVmean, these observations justified the removal of SUVmean from the multivariate analyses and the inclusion of SUVmax.

The examination of SUVmax and volume with the tumor model aimed to ensure that analyses involving these variables were not merely surrogates for the tumor model. No significant differences were observed between SUVmax values and the tumor model, confirming the substantial variation in data among tumor models. Regarding volume, no significant differences were found between the MLM1 model and the other two; however, MOC1 and MOC2 exhibited significant differences between each other, again consistent with the literature [18]. With the MLM1 model volume being insignificant compared to the other two, there appears to be enough inter-model volume variability to not result in volume being a strong predictor of the model. These analyses support SUVmax and volume's independence as factors, further validating their distinct contributions in the analytical context.

The coefficient of variance was examined concerning liver normalization to assess the viability of using this organ in the mice as a normalization factor. In many human studies, SUV normalization relied on the blood pool in the heart. However, in mice, the size of the heart and the resolution of the scanner made it impractical, as muscle activity from the heart wall interfered with any blood pool ROIs taken. According to literature, the liver could also serve as a valid organ for SUV normalization as it is more feasible in this small animal study due to the organ's size [11]. The resulting mean coefficient of variation among all mice for liver SUV measurements was 16%, with the maximum reaching 35%, which were both deemed acceptable. The

combination of a literature review and the resulting coefficients of variation justified using this normalization method in the subsequent multivariate analysis.

4.2.4 Multivariate Survival Analysis - Cox Proportional Hazards Model

Analyzing the Cox proportional hazards model coefficients for SUVmax (0.0524) and volume (0.0150), both variables have been identified as positive indicators of a worse prognosis because they are >0. The resulting hazard ratio for SUVmax indicates that with every 1-unit increase in SUVmax value, there is a 5.4% increase in hazard. Similarly, there is a 1.5% increase in hazard for every cubic millimeter increase in the volume of the tumor. The Cox proportional hazards model results in a significant difference in overall survival when split using the median risk score. This finding further supports the hazard ratio analysis of each covariate as a prognostic factor.

4.3 Future Directions

4.3.1 Multiscale Analyses

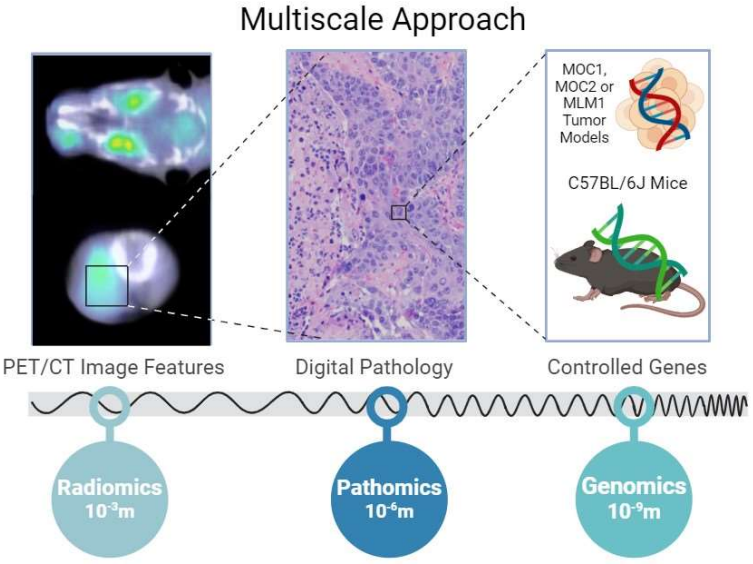

Figure 21. Multiscale approach of chemoradiation resistance analysis using mouse models.

The next step of this research involves extracting a comprehensive radiomics panel and identifying additional image biomarkers that can offer prognostic information for this dataset. In this thesis, SUVmax and SUVmean, both of which are first-order histogram radiomic features, along with ROI volume, a shape-based feature, were investigated [14]. However, this only brushes the surface of all radiomic features that could be explored.

Texture radiomic features characterize intensity fluctuations across the image [14, 15]. Fine texture features analyze adjacent voxel pairs and the frequency of intensity co-occurrence [15]. Coarse texture features examine larger-scale heterogeneities, focusing on the size of consecutive voxels with the same intensities [15].

Literature suggests that homogeneous coarse textures within CT regions of interest (ROIs) are associated with elevated rates of local recurrence in lung cancers, indicating prognostic significance in CT texture radiomics [15]. Furthermore, metabolic texture radiomics in head and neck cancer using PET images indicate that increased homogeneity in FDG uptake is correlated with better prognosis [4]. Guided by these studies, conducting a comprehensive texture radiomics analysis on both the CT and PET scans in this dataset represents the next research phase to explore potential associations between tumor texture and density, metabolic activity textures, and mouse outcomes.

Moving to a finer scale, pathomic analyses will involve examining the tissue samples obtained during necropsy. Utilizing digital pathology, pathomics focus on deriving computational measurements and features from histopathological images that may be challenging or impossible to discern by the human eye [28]. This provides insights into tumor immune responses and their prognostic implications. Immune dysregulation significantly influences the development and progression of head and neck squamous cell carcinomas [29]. Improved understanding of the tumor microenvironment could further guide research in immunotherapies.

One specific area of interest in pathomics is the spatial distribution and quantity of tumor-infiltrating lymphocytes, which have demonstrated prognostic significance in non-small cell lung cancers [28, 30]. Other pathomic features encompass cell texture and shape, as well as local and global structures, including patterns of cell types and proteins such as collagen [28]. In addition to examining tumor-infiltrating lymphocytes, exploring other immune cells both within the tumor and at the tumor-stroma boundary through pathomic analyses presents an intriguing avenue for investigating prognostic relevance.

Transitioning to the finest scale, the flash-frozen tissue samples obtained during necropsy can serve as material for transcriptomic and genomic analyses. In this study, gene regulation in mice was strictly controlled by employing only C57BL/6J mice, and low-passage cancer cultures were utilized to minimize the introduction of additional mutations. Transcriptomic analysis will assess the gene expression patterns which can then be correlated with tumor phenotypes [31].

Exploring potential associations among the multi-scale "-omic" features is an area of research interest. A long-term objective is to understand the biological origins of prognostic signals, with contributions from radiomics, pathomics, transcriptomics, genomics, and their interconnectedness. Understanding the biological underpinnings of prognostic signals can provide valuable insights into future research directions aimed at addressing chemoradiation resistance in a more targeted manner.

4.3.2 Future Mouse Models

Utilizing genetically engineered mouse models and exposing them to known carcinogens responsible for human head and neck cancer, such as benzo[a]pyrene (BaP) found in cigarettes and pollution, can induce genetically diverse cancers in mice that more closely resemble the diversity and etiology of human head and neck cancers [32]. An added advantage of this model over the transplant models utilized in this thesis is that the cancer cells will not be foreign to the

mouse, thereby mitigating potential effects on the tumor microenvironment due to immune recognition of foreign transplant cells. One method of genetic modification of mice involves altering gene expression or deletion using Cre-type site-specific recombinases, such as Cre recombinase from bacteriophage P1, which induce targeted DNA rearrangements between loxP sequences [33]. Mutations with potential benefits could include the deletion of p53, as HNSCC often exhibits mutations in this gene [1, 34].

Immune knockout models involve disrupting genes associated with specific immune functions. Repeating this experiment using various knockout models, where certain immune cells are absent, could yield deeper insights into the roles played by specific immune cells in cancer progression, therapy response, and the characteristics observed through radiomic and pathomic analyses. This approach can enhance our understanding of the biological mechanisms behind radiomic signals and the contributions of individual immune system components.

5. Conclusions

The implementation of a sophisticated preclinical head and neck squamous cell carcinoma mouse model, with a large sample size and diverse range of responses and outcomes, has resulted in a multivariate model supporting the hypothesis that SUVmax data from micro-PET imaging and volume data from micro-CT imaging, acquired 2 weeks post-treatment initiation, can offer prognostic insights into overall survival and chemoradiation therapy resistance. Utilizing small animal imaging systems and preclinical tumor models provides an experimental framework to assess imaging biomarkers, enhancing our understanding of the radiomic expression underlying chemoradiation resistance in head and neck cancers.

Appendix A

A.1 Media Recipes and Stock Solutions

MOC Media Recipe

- 500 mL IMDM
- 250 mL Ham's F12
- 37.5 mL FBS
- 7.5 mL pen/strep
- 900 µL hydrocortisone (0.33 µg/ µL stock, Sigma H0888-1 g)
- 375 µL insulin (10 ug/ µL stock, Sigma I6334-100 mg)
- 19 µL EGF (0.2 µg/ µL stock, Gibco PHG0311, 100 mg)
- 1 L sterile filter flask

Procedure:

1. Add all components except F12 to the IMDM media bottle.
2. In a 1 L sterile filter flask, filter F12 and the IMDM solution.
3. Date and label the bottle as 'MOC Media Complete.'

mEERL/MLM Media Recipe

- 338 mL DMEM
- 112 mL Ham's F12
- 50 mL FBS
- 5 mL pen/strep (Invitrogen 15140-122)
- 10 µL hydrocortisone (25 µg/ µL stock, Sigma H0396-100mg)

- 250 µL insulin (10 µg/ µL stock, Sigma I6634-250 mg)

- 125 µL EGF (0.2 µg/ µL stock, Gibson PHG0311- 100 mg)

- 100 µL transferrin (25 µg/ µL, Sigma T1147-100 mg)

- 3.4 µL tri-iodo-thyronine (0.2 µg/µL, T5516-1 mg)

- 1 L sterile filter flask

Procedure:

1. Add all components except F12 to DMEM media bottle.

2. In a 1 L sterile filter flask, filter F12 and the DMEM solution.

3. Date and label the bottle as 'mEERL/MLM Media Complete.'

Making Stocks:

Insulin Stock @ 10 µg / µL (Sigma I6634-100 mg)

In TC hood:

1. Add 10 mL sterile H2O to 100 mg bottle of insulin.

2. Add 100 µL 1N HCl to dissolve insulin. Add more if needed.

3. Filter through 0.2 um sterile filter.

4. Aliquot 400 µL into twenty-five 1 mL Eppendorf tubes.

5. Store at -20°C.

EGF Stock @ 0.2 µg/µL (Gibco PHG0311 100mg)

1. Centrifuge powder to the bottom of the bottle.

2. In TC hood, add 500 µL sterile PBS to 100 µg bottle of EGF.

3. Aliquot 25 µL into twenty 1 mL Eppendorf tubes.

4. Store at -20°C.

Hydrocortisone Stock @ 0.33 mg/mL (Sigma H0888-1g)

In TC hood:

1. Regardless of final stock concentration, add 1 mL absolute ethanol per 1 mg of hydrocortisone. Gently swirl to dissolve.

2. Add 2 mL sterile serum-free medium with mixing.

3. Aliquot 1 mL into three 1.5 mL Eppendorf tubes.

4. Store at -20°C.

Insulin Stock @ 10 µg/µL (Sigma I6634-100 mg)

In TC hood:

1. Add 10 mL sterile H2O to 100 mg bottle of insulin.

2. Add 100 µL 1N HCl to dissolve insulin. Add more if needed.

3. Filter through 0.2 µm sterile filter.

4. Aliquot 400 µL into twenty-five 1 mL Eppendorf tubes.

5. Store at -20°C.

EGF Stock @ 0.2 µg/ µL (Gibco PHG0311 100mg)

1. Centrifuge powder to the bottom of the bottle.

2. In TC hood, add 500 µL sterile PBS to 100 µg bottle of EGF.

3. Aliquot 25 µL into twenty 1 mL Eppendorf tubes.

4. Store at -20°C.

Hydrocortisone Stock @ 25 µg/µL (Sigma H0396-100mg)

In TC hood:

1. Regardless of the final stock concentration, add 4 mL sterile H2O to 100 mg bottle of hydrocortisone. Gently swirl to dissolve.

2. Aliquot 1 mL into three 1.5 mL Eppendorf tubes.

3. Store at -20°C.

Note: Always handle stock solutions in a sterile environment and follow laboratory safety guidelines.

Works Cited

[1] M. E. Sabatini and S. Chiocca, "Human papillomavirus as a driver of head and neck cancers," *British Journal of Cancer,* pp. 306-314, 2020.

[2] D. E. Johnson, B. Burtness, C. R. Leemans, V. W. Y. Lui, J. E. Bauman and J. R. Grandis, "Head and Neck Squamous Cell Carcinoma," *Nature Reviews Disease Primers,* vol. 6, 2020.

[3] P. Economopoulou, I. Kotsantis and A. Psyrri, "Special Issue about Head and Neck Cancers: HPV Positive Cancers," *International Journal of Molecular Sciences,* vol. 21, no. 9, 2020.

[4] K. J. Lafata, Y. Chang, C. Wang, Y. M. Mowery, I. Vergalasova, D. Niedzwiecki, D. S. Yoo, J.-G. Liu, D. M. Brizel and F.-F. Yin, "Intrinsic radiomic expression patterns after 20 Gy demonstrate early metabolic response of oropharyngeal cancers," *Medical Physics,* vol. 48, no. 7, pp. 3767-3777, 2021.

[5] L. M. Teigen, A. J. Kuchnia, M. Mourtzakis and C. P. Earthman, "The Use of Technology for Estimating Body Composition," *Nutrition in Clinical Practice,* vol. 32, no. 1, pp. 20-29, 2016.

[6] A. Al-Ibraheem, A. Buck, B. J. Krause, K. Scheidhauer and M. Schwaiger, "Clinical Applications of FDG PET and PET/CT in Head and Neck Cancer," *Journal of Oncology,* 2009.

[7] L. Kostakoglu, H. Agress, Jr and S. J. Goldsmith, "Clinical Role of FDG PET in Evaluation of Cancer Patients," *RadioGraphics,* vol. 23, no. 2, 2003.

[8] D. W. Townsend, "Physical Principles and Technology of Clinical PET Imaging," *Annals of the Academy of Medicine, Singapore,* vol. 33, no. 2, pp. 133-145, 2004.

[9] P. E. Kinahan and J. W. Fletcher, "Positron emission tomography-computed tomography standardized uptake values in clinical practice and assessing response to therapy," *Semin Ultrasound CT MR,* vol. 31, no. 6, pp. 496-505, 2010.

[10] H. A. Ziessman, J. P. O'Malley and J. H. Thrall, Eds., "Oncology: Positron Emission Tomography," in *Nuclear Medicine*, 4th ed., 2014, pp. 227-264.

[11] N. H. M. Azmi, S. Suppiah, C. W. Liong, N. M. Noor, S. M. Said, M. H. Hanafi, C. Kaewput, F. F. A. Saad and S. Vinjamuri, "Reliability of standardized uptake value normalized to lean body mass using the liver as a reference organ, in contrast-enhanced 18F-FDG PET/CT imaging," *Radiation Physics and Chemistry,* vol. 147, pp. 35-39, June 2018.

[12] J. Shur, S. J. Doran, S. Kumar, D. A. Dafydd, K. Downey, J. P. O'Connor, N. Papanikolaou, C. Messiou, D. Koh and M. Orton, "Radiomics in Oncology: A Practical guide," *Radiographics,* vol. 41, no. 6, pp. 1717-1732, 2021.

[13] K. J. Lafata, Y. Wang, B. Konkel, F.-F. Yin and M. R. Bashir, "Radiomics: a primer on high-throughput image phenotyping," *Abdominal Radiology (New York),* vol. 47, no. 9, pp. 2986-3002, 2022.

[14] M. E. Mayerhoefer, A. Materka, G. Langs, I. Häggström, P. Szczypiński, P. Gibbs and G. Cook, "Introduction to Radiomics," *Journal of Nuclear Medicine,* vol. 61, no. 4, pp. 488-495, April 2020.

[15] K. J. Lafata, J. C. Hong, R. Geng, B. G. Ackerson, J.-G. Liu, Z. Zhou, J. Torok, C. R. Kelsey and F.-F. Yin, "Association of pre-treatment radiomic features with lung cancer recurrence following stereotactic body radiation therapy," *Physics in Medicine & Biology,* vol. 64, no. 2, 8 January 2019.

[16] W. W. LaMorte, "Cox Proportional Hazards Regression Analysis," Boston University School of Public Health, 3 June 2016. [Online].

[17] E. Zurita, M. Chagoyen, M. Cantero, R. Alonso, A. Gonzalez-Neira, A. Lopez-Jimenez, J. A. Lopez-Moreno, C. P. Landel, J. Benitez, F. Pazos and L. Montoliu, "Genetic polymorphisms among C57BL/6 mouse inbred strains," *Transgenic Research,* vol. 20, pp. 481-489, 2011.

[18] N. P. Judd, C. T. Allen, A. E. Winkler and R. Uppaluri, "Comparative analysis of tumor-infiltrating lymphocytes in a syngeneic mouse model of oral cancer," *Otolaryngology - Head and Neck Surgery ,* vol. 147, no. 3, pp. 493-500, 2012.

[19] F. Castellino and R. N. Germain, "COOPERATION BETWEEN CD4+ AND CD8+ T CELLS: When, Where, and How," *Annual Review of Immunology,* vol. 24, pp. 519-540, 2006.

[20] R. V. Luckheeram, R. Zhou, A. D. Verma and B. Xia, "CD4+T Cells: Differentiation and Functions," *Journal of Immunology Research,* 2012.

[21] J. Neefjes, M. L. M. Jongsma, P. Paul and O. Bakke, "Towards a systems understanding of MHC class I and MHC class II antigen presentation," *Nature Reviews Immunology,* vol. 11, pp. 823-836, 2011.

[22] S. Ryzhov, V. S. Novitskiy, A. E. Goldstein, A. Biktasova, M. R. Blackburn, I. Biaggioni, M. M. Dikov and I. Feoktistov, "Adenosinergic Regulation of the Expansion and Immunosuppressive Activity of CD11b+Gr1+ Cells," *the Journal of Immunology,* vol. 187, no. 11, pp. 6120-6129, 2011.

[23] D. W. Vermeer, J. D. Coppock, E. Zeng, K. M. Lee, W. C. Spanos, M. D. Onken, R. Uppaluri, J. H. Lee and P. D. Vermeer, "Metastatic model of HPV+ oropharyngeal squamous cell carcinoma demonstrates heterogeneity in tumor metastasis," *Oncotarget,* vol. 7, no. 17, pp. 24194-24207, 2016.

[24] J. C. J. Wei, G. A. Edwards, D. J. Martin, H. Huang, M. L. Crichton and M. A. F. Kendall, "Allometric scaling of skin thickness, elasticity, viscoelasticity to mass for micro-medical device translation: from mice, rats, rabbits, pigs to humans," *Scientific Reports,* vol. 7, 2017.

[25] R. Forghani, M. Levental, R. Gupta, S. Lam, N. Dadfar and H. D. Curtin, "Different Spectral Hounsfield Unit Curve and High-Energy Virtual Monocromatic Image Characteristics of Squamous Cell Carcinoma Compared with Nonossified Thyroid Cartilage," *American Journal of Neuroradiology,* vol. 36, no. 6, 2015.

[26] J. Yep, N. Hall, D. W. Townsend, J. Wall, A. Solomon, J. W. Kabalka, S. Kennel, D. F. Newport, S. Siegel, D. Bailey, A. Smith and R. E. Nutt, "Combined clinical PET/CT and microPET small animal imaging," in *IEEE Nuclear Science Symposium Conference Record*, 2004.

[27] J. M. Pimiento, A. H. Davis-Yadley, R. D. Kim, D.-T. Chen, E. A. Eikman, C. G. Berman and M. P. Malafa, "Metabolic Activity by (18)F-FDG-PET/CT is Prognostic for Stage I and II Pancreatic Cancer," *Clinical Nuclear Medicine,* vol. 41, no. 3, pp. 177-181, 2016.

[28] C. Lu, R. Shiradkar and Z. Liu, "Integrating pathomics with radiomics and genomics for cancer prognosis: A brief review," *Chinese Journal of Cancer Research,* vol. 33, no. 5, pp. 563-573, 31 October 2021.

[29] R. L. Ferris, "Immunology and Immunotherapy of Head and Neck Cancer," *Journal of Clinical Oncology,* vol. 33, no. 29, pp. 3293-3304, 10 October 2015.

[30] G. Corredor, X. Wang, Z. Yu, C. Lu, P. Fu, K. Syrigos, D. L. Rimm, M. Yang, E. Romero, K. A. Schalper, V. Velcheti and A. Madabhushi, "Spatial architecture and arrangement of tumor-infiltrating lymphocytes for predicting likelihood of recurrence in early-stage non-small cell lung cancer," *Clinical Cancer Research,* vol. 25, no. 5, pp. 1526-1534, 1 March 2019.

[31] L. Badea and E. Stănescu, "Identifying transcriptomic correlates of histology using deep learning," *PLoS One,* 25 November 2020.

[32] T. Souza, D. Jennen, J. van Delft, M. van Herwijnen, S. Kyrtoupolos and J. Kleinjans, "New insights into BaP-induced toxicity: role of major metabolites in

transcriptomics and contribution to hepatocarcinogenesis," *Archives of Toxicology,* vol. 90, pp. 1449-1458, 2016.

[33] J. Hoersten, G. Ruiz-Gómez, F. Lansing, T. Rojo-Romanos, L. T. Schmitt, J. Sonntag, M. T. Pisabarro and F. Buchholz, "Pairing of single mutations yields obligate Cre-type site-specific recombinases," *Nucleic Acids Research,* vol. 50, no. 2, pp. 1174-1186, 25 January 2022.

[34] C.-L. Lee, Y. M. Mowery, A. R. Daniel, D. Zhang, A. B. Sibley, J. R. Delaney, A. J. Wisdom, X. Qin, X. Wang, I. Caraballo, J. Gresham, L. Luo, D. van Mater, K. Owzar and D. G. Kirsch, "Mutational landscape in genetically engineered, carcinogen-induced, and radiation-induced mouse sarcoma," *JCI Insight,* vol. 4, no. 13, 11 July 2019.

[35] J. J. Schreiber, P. A. Anderson, H. G. Rosas, A. L. Buccholz and A. G. Au, "Hounsfield Units for Assessing Bone Mineral Density and Strength: A Tool for Osteoporosis Management," *The Journal of Bone & Joint Surgery,* vol. 93, no. 11, pp. 1057-1063, 2011.

[36] S. Kim, G. H. Lee, S. Lee, S. H. Park, H. B. Pyo and J. S. Cho, "Body fat measurement in computed tomography image," *Biomedocal Sciences Instrumentation,* pp. 303-308, 1999.